Galactic scaled down versions of extragalactic AGNs

Mirabel (2002)

Microquasar	Quasar	Collapsar
Companion star		
Relativistic jet	UV and visible	X-rays, visible, then radio
X-rays	Radio, X-rays	Radio, X-rays
Stellar-mass black hole	Supermassive black hole	Stellar-mass black hole
Accretion disk (1,000 km diameter)	Accretion disk (1 billion km)	Accretion disk (100 km)
Light-years	Millions of light-years	Light-hours
	Host galaxy	Helium / Hydrogen

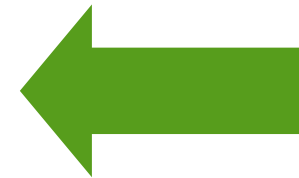Microblazar   Blazar   Gamma ray burst

Suggested readings:

- Mirabel & Rodriguez 1999, ARAA, 37, 409 – 443

- Fender & Belloni 2004, ARAA, 42, 317 – 364

- Mirabel 2007, astro-ph/0701837

- Fender & Muñoz-Darias 2015, http://arxiv.org/pdf/1505.03526.pdf

- Fanti & Fanti, Cap. 27
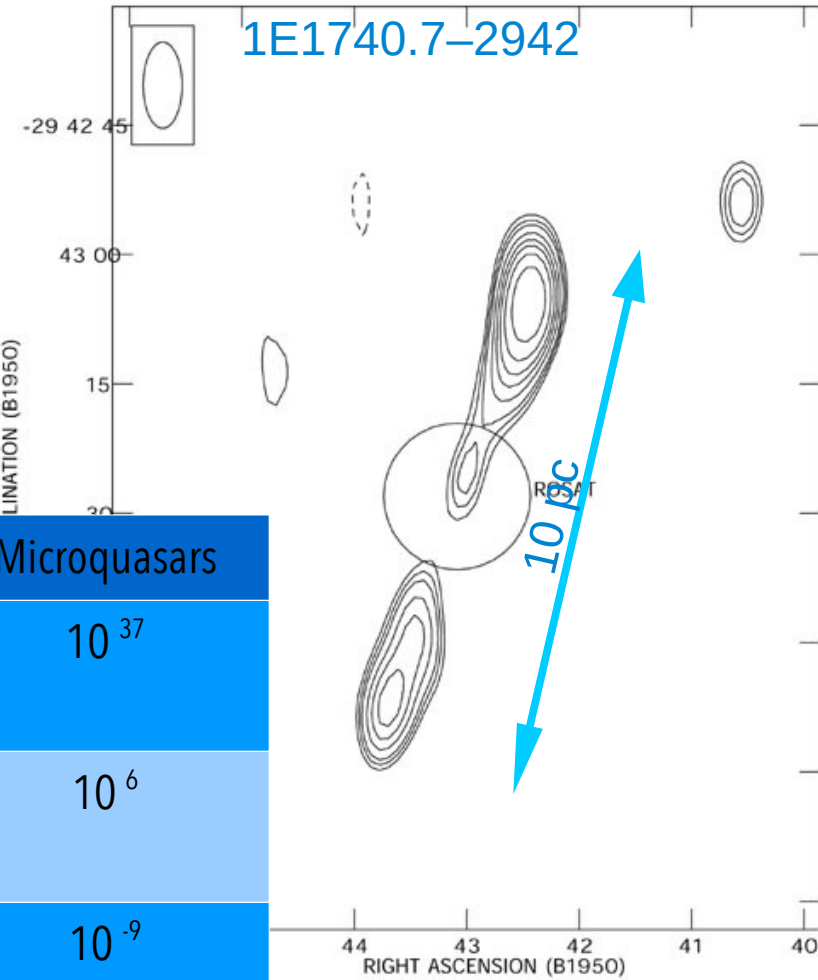
Scaled version of AGN engines. With some advantages:

$$R_{Sch} = \frac{2\,GM_{BH}}{c^2} \qquad \text{and} \qquad \Delta t \approx M_{BH}$$

- Microquasars .vs. Quasars in the radio domain

3C244.1

300 kpc

1E1740.7−2942

10 pc
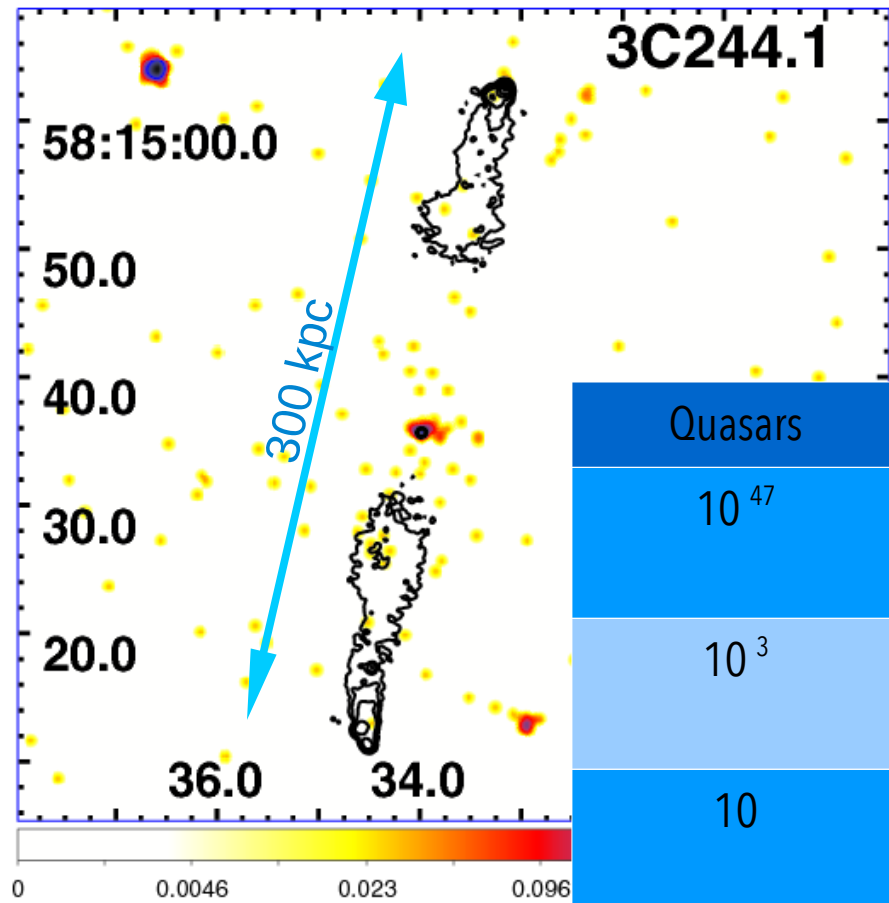
Quasars		Microquasars
10^{47}	Luminosity (erg s^{-1})	10^{37}
10^3	T of Acc. Disk (^{o}K)	10^6
10	Accretion rate (M$_{\odot}$ yr^{-1})	10^{-9}
10^6	Jet length (pc)	a few
$10^7 - 10^9$	BH mass (M$_{\odot}$)	1 − 10

Binaries with a "normal" star & collapsed body

WD – Cataclismic Variables [(recurrent) novae] (not discussed here)

NS (e.g. Sco X-1) or **BH** (e.g. Cyg X-1) – **Micro-quasar**, recognized as XRBs

Donor determines subclasses in XRBs:

➢ LMXRBs
  Pop II (old) stars (main sequence, RG) overflowing the Roche lobe:
  Lagrangian point accretion. The vast majority of the radiation comes into the X-rays,
 nearly invisible in the optical

➢ HMXRBs
  Pop I (young) stars (O, B, Be, blue supergiant) losing mass via stellar wind
  (a fraction captured by the NS/BH). Donor bright in the optical

Intermediate Mass X-Ray Binaries (IMXRBs): donor is an intermediate mass star

Microquasars: (accreting galactic X-ray binaries with)

➔ Two sided[contrary to most AGN] relativistic (v >0.3 c) jets

➔ Accretion disk onto compact object

➔ (Radio) non-thermal radiation

➔ Variability on a variety of timescales (often erratic)

➢ Physical and morphological properties similar to AGN , but much shorter time scale
➢ Time evolution related to changes in the disk-jet system, inflow – outflow processes
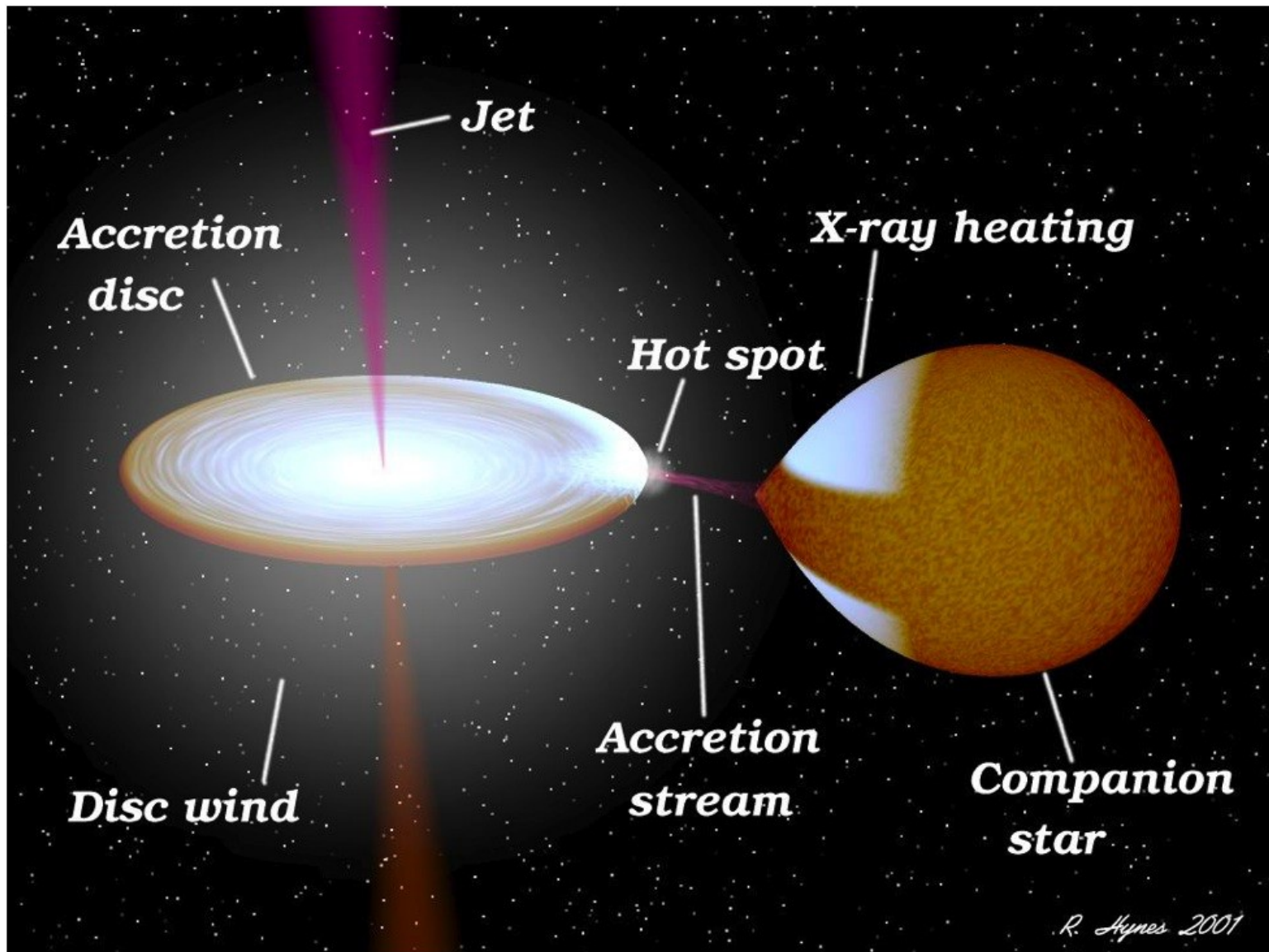
XRB distribution
within our Galaxy
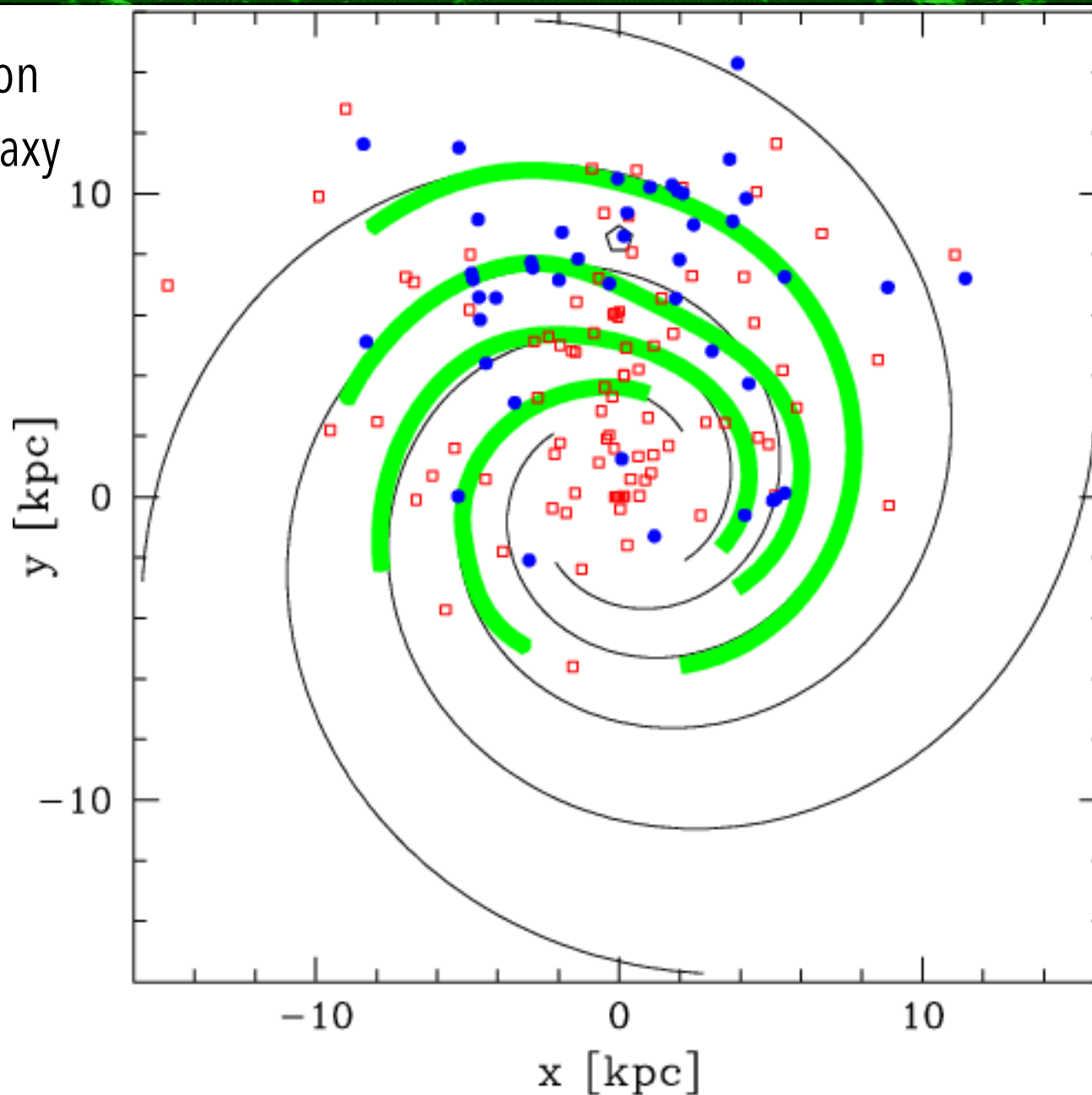
Face-on view of the distribution of low mass (open squares) and high mass (filled circles) X-ray binaries in our Galaxy.
The origin of the coordinate is at the Galactic Centre. The Sun (pentagon) is located at $x=0$, $y=8.5$ kpc. (From Grimm et al. 2002)

- Ingredients in a LMXRB:

   A collapsed body (NS – BH)

   A MS (RG) companion star, with Roche lobe overflow

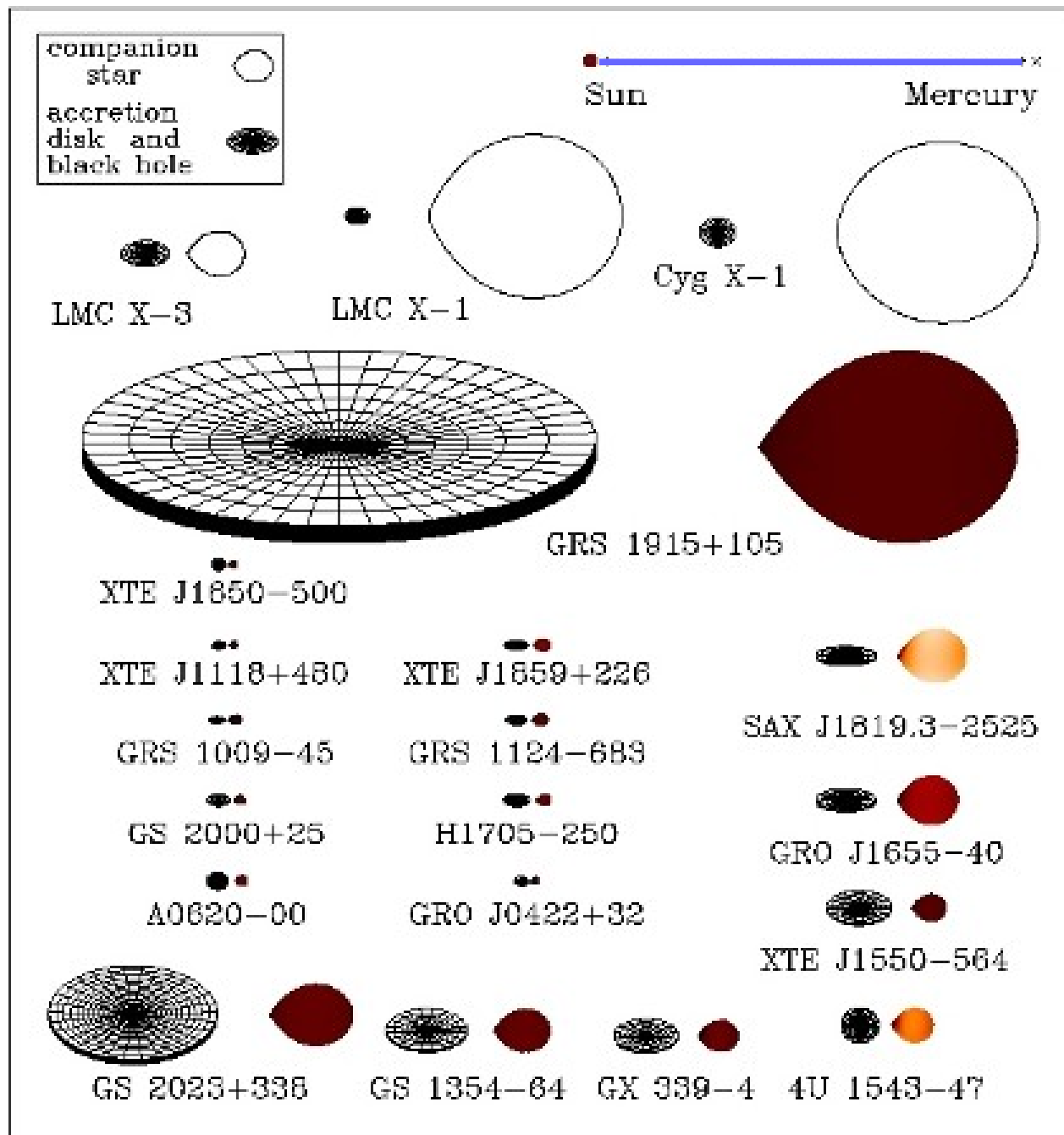- Ingredients in a HMXRB:

    A collapsed body (NS – BH)

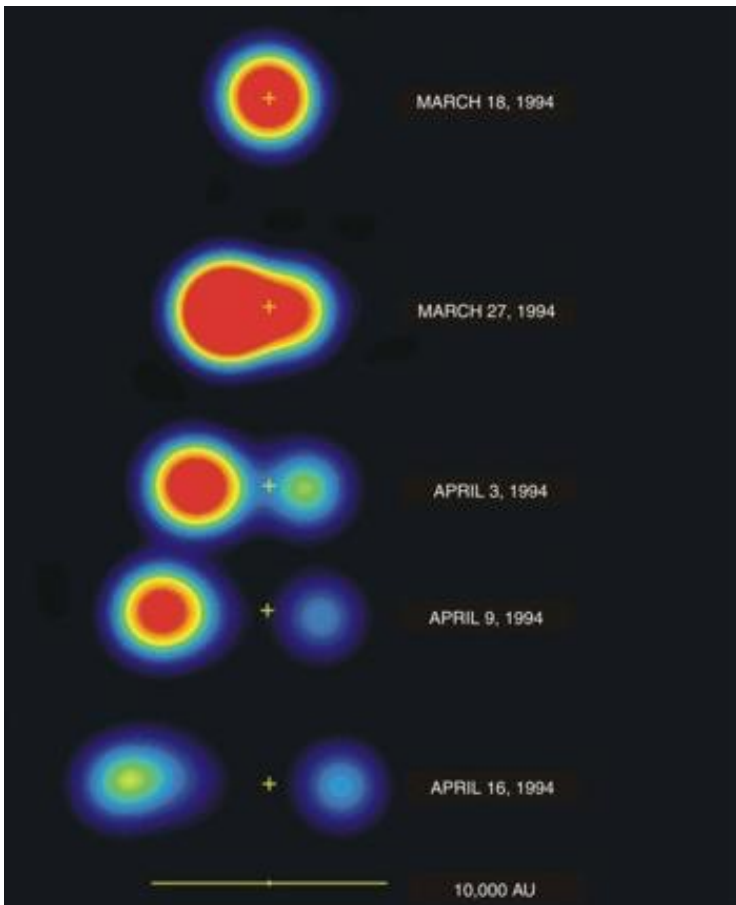   A massive companion star, with substantial mass loss via stellar wind.

Most of the action takes place here, where either the NS or the BH is.

- Ingredients: the companion star provides the gas (via Roche Lobe overflow in LMXRBs, via stellar wind in HMXRBs): an accretion disk is formed, with a hot corona around the compact object. A jet is generated perpendicularly to the accretion disk

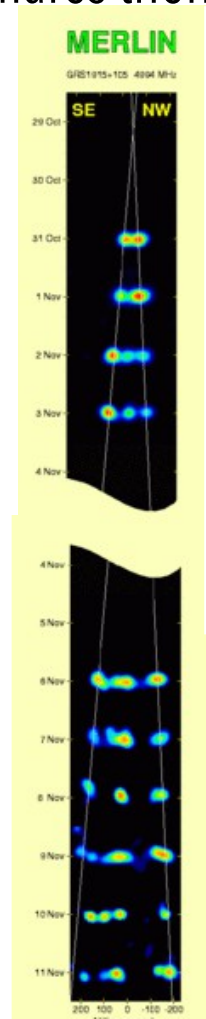A few well known objects, most with a BH: SS433, GRS1905+105, Cyg X-1

Constraints from (early) observations:

- Discovered in August 1992 (WATCH all sky monitor on board of GRANAT)
- Radio: Asymmetric brightness due to Doppler effects
- Measured $v_{app} \sim 1.25\,c$ (1994), bulk speed 0.92c, i=70deg (Mirabel & Rodriguez 1999)
- Multi-λ monitoring campaigns to correlate variability: highly variable, repeated flares then periods of quiescence

VLBI & MERLIN (consecutive days)

MARCH 18, 1994

MARCH 27, 1994

APRIL 3, 1994

APRIL 9, 1994

APRIL 16, 1994

10,000 AU

MERLIN

GRS1915+105 4994 MHz

SE   NW

29 Oct
30 Oct
31 Oct
1 Nov
2 Nov
3 Nov
4 Nov
4 Nov
5 Nov
6 Nov
7 Nov
8 Nov
9 Nov
10 Nov
11 Nov

GRS 1915+105:

The most prominent microquasar (?) showing dramatic variability in its light curve, quasi-periodic oscillations, phase lags, and coherence behavior. It is the most energetic object known in our galaxy, with a luminosity of 5×10^{39} ergs s^{-1} in the high state and 10^{38} ergs s^{-1} in the low state.

Binary system: @ 12 kpc, contains a 1 M☉ late-type giant in a 33.5 day orbit around a 14 M☉ BH

RXTE study of GRS1915+105

Monitored by RXTE for more than a decade: in a stable state (Rau & Greiner, 2003, A&A, 397, 711) during most of the first four years, and its spectrum was dominated by a hard power-law shaped component arising from inverse Compton scattering of soft disk photons on a thermally dominated hybrid corona above the accretion disk.

Radio flux densities at 2.25 GHz and 15 GHz correlate with the power law slope, thus revealing a connection between the outflowing matter and the comptonizing region.

A 590 day long-term quasi-periodicity was found in X-rays and radio, possibly originating from a precession of a radiation-induced warp in the accretion disk (Rau et al., 2003, ApJ, 590, L37).

It exhibits a wide range of quasi-periodic oscillations (QPOs), with central frequencies in the range 0.01-10 Hz. The amplitude and frequency of the QPOs appear to be strongly correlated with the spectral state of GRS 1915+105
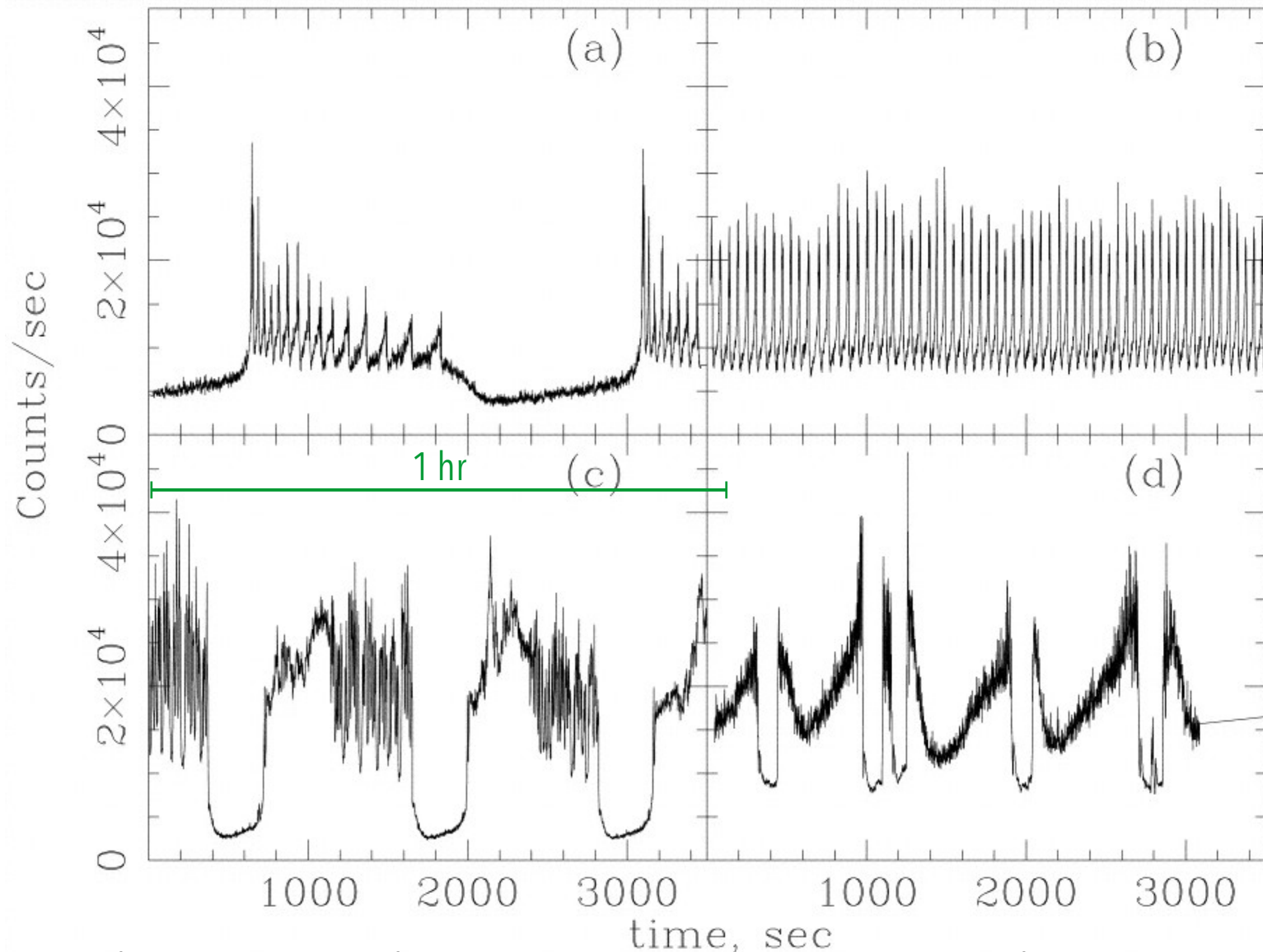

Selected segments of the X-ray light curve of GRS 1915+105, demonstrating the broad range of variability patterns in this unusual source. The data were obtained from the public archive of the *Rossi X-Ray Timing Explorer* (*RXTE*). (Nayakshin et al. 200)
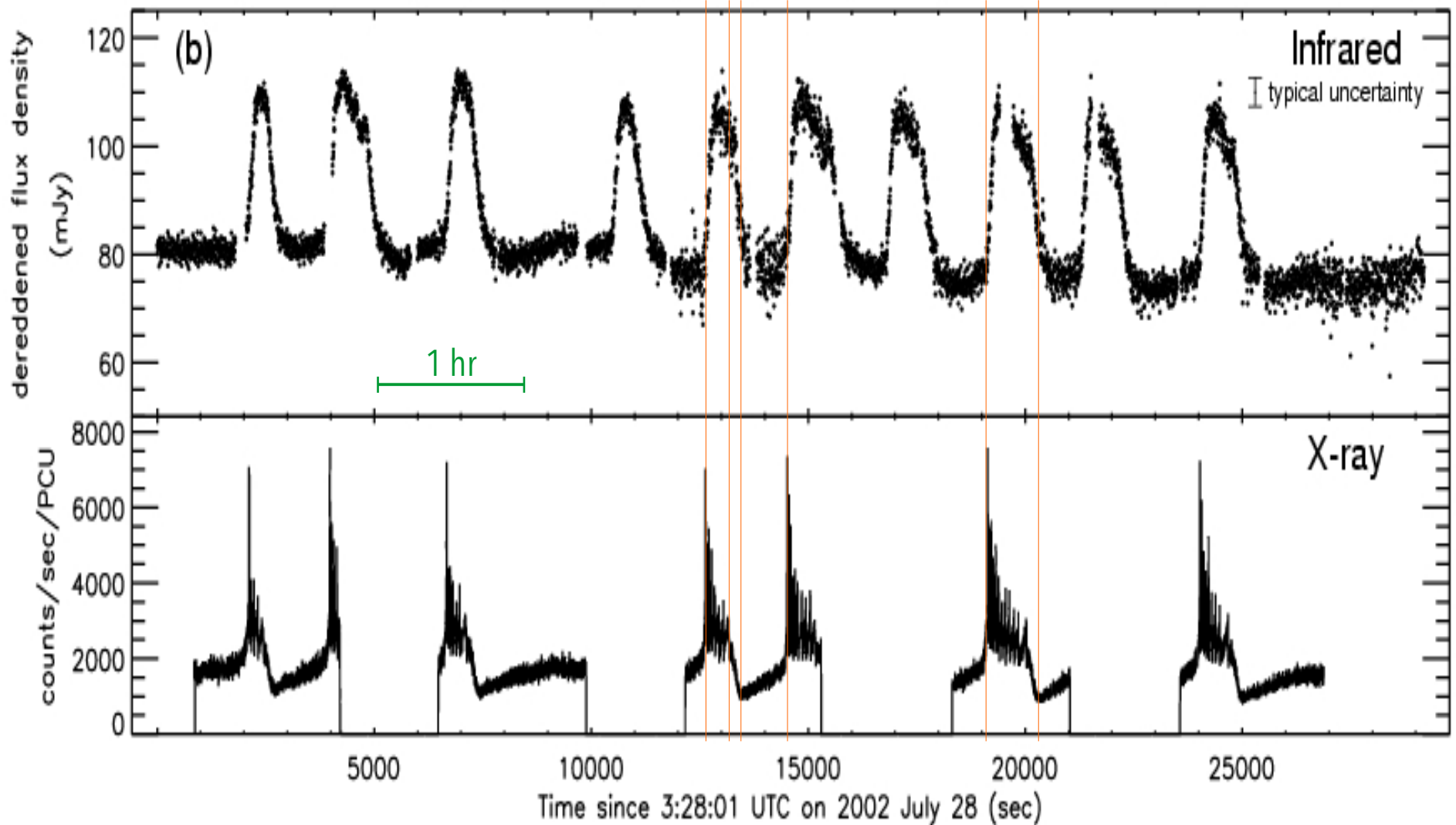
Simultaneous IR (jet) and X-ray observations of GRS 1915+105 show
jet ejection is tightly correlated with rapid disappearance of accretion disk.
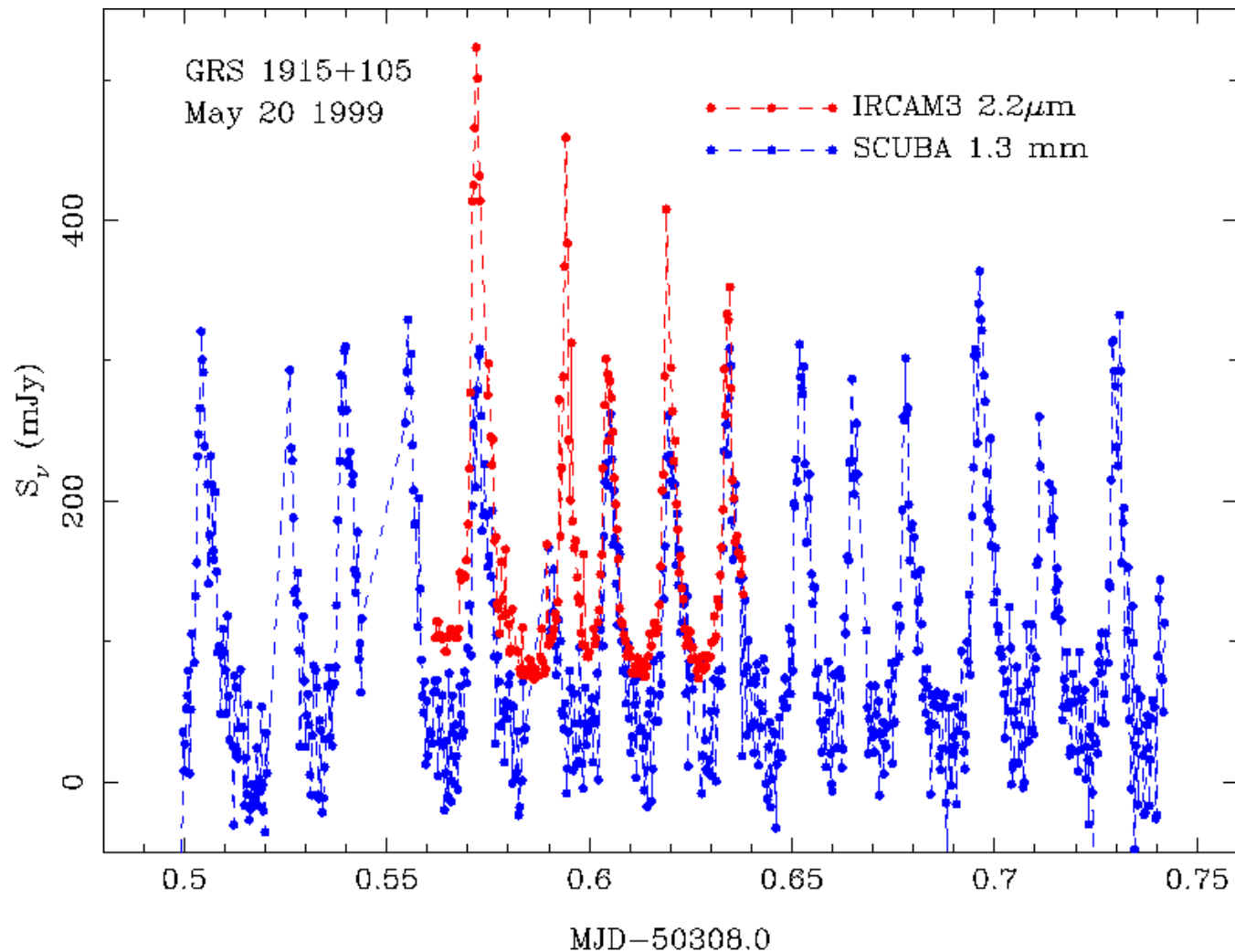
Large, repeated synchrotron flares observed at mm (blue) and infrared (red) wavelengths from the black hole binary GRS 1915+105. The figure shows a sequence of 16 quasi-periodic flaring events observed at mm wavelengths, five of which are simultaneously detected in the infrared band. From Fender & Pooley (2000).
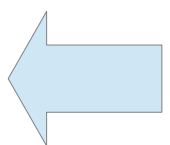
Microquasars (et al.)
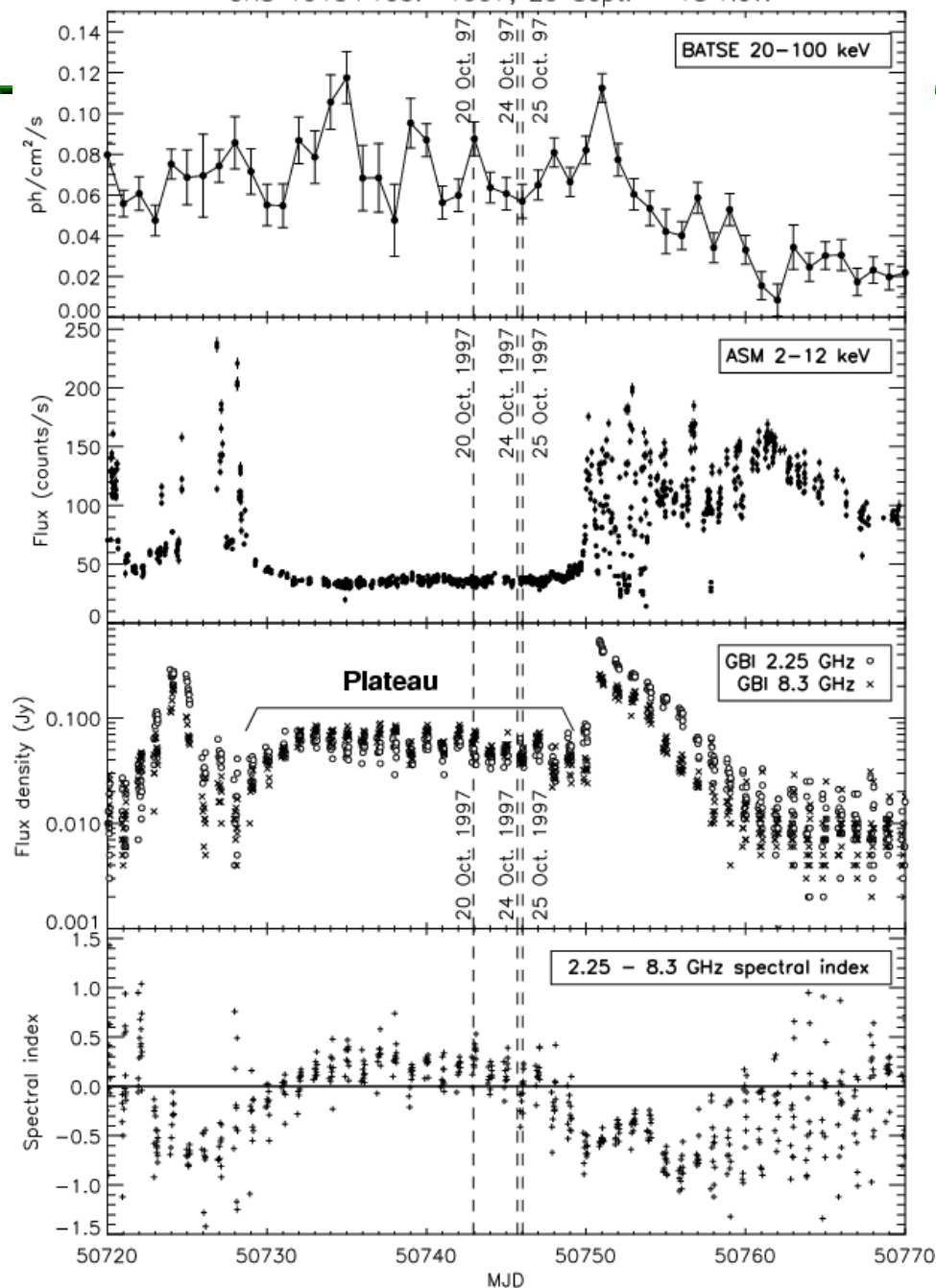
Fuchs et al. (2003): X-ray and radio flux monitoring of GRS 1915+105 around October 24 1997 (MJD 50745). The upper panels show the photon flux measured by BATSE in the 20-100 keV band and the integrated count rate in the 2-12 keV band by RXTE. The lower panels show the corresponding flux densities measured at 2.25 GHz and 8.3 GHz with the (GBI) and the spectral index from these two frequencies. On the latter plot zero has been marked with a solid line in order to emphasize the optically thick ($\alpha \sim 0$) radio emission of the plateau state.

Simultaneous IR (jet) and X-ray observations of GRS 1915+105 show jet ejection is tightly correlated with rapid disappearance of accretion disk.
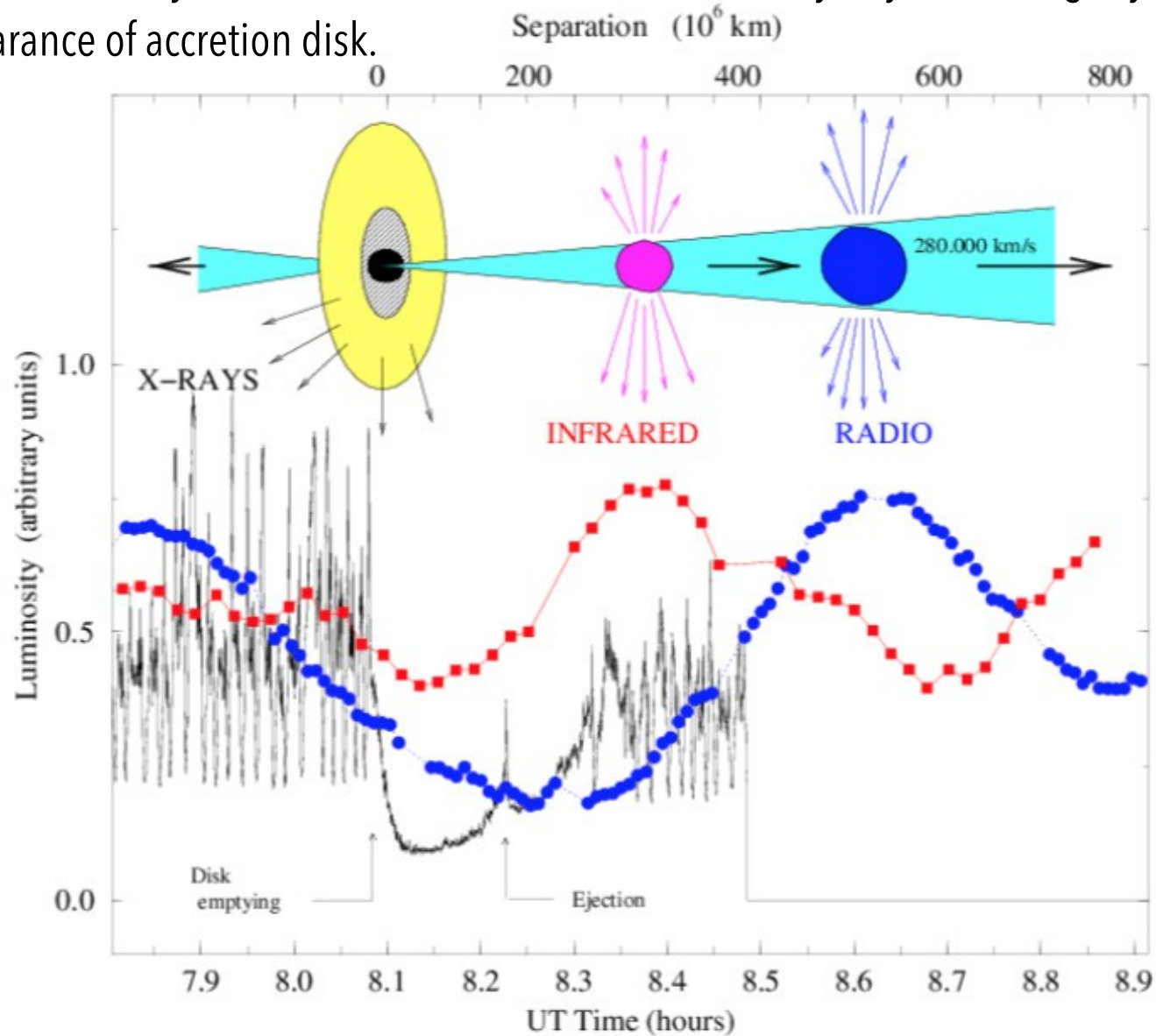

Observation of the link between accretion and ejection. X-ray, NIR & radio light curves of GRS 1915+105 during the 1997 Sep. 9 multi-λ campaign. The disappearance of the internal part of the disk (decrease in the X-ray flux) is followed by ejection of relativistic plasma clouds (Chaty 1998; Mirabel et al. 1998).

Microquasars: SS433

Large scale structure (PSF ~ 1')
SNR W50 with two elongations
Nearly uniform spix

SS433/W50 HBA

19098+05   1464.900 MHZ

Two-point spectral index map (140–1465 MHz)
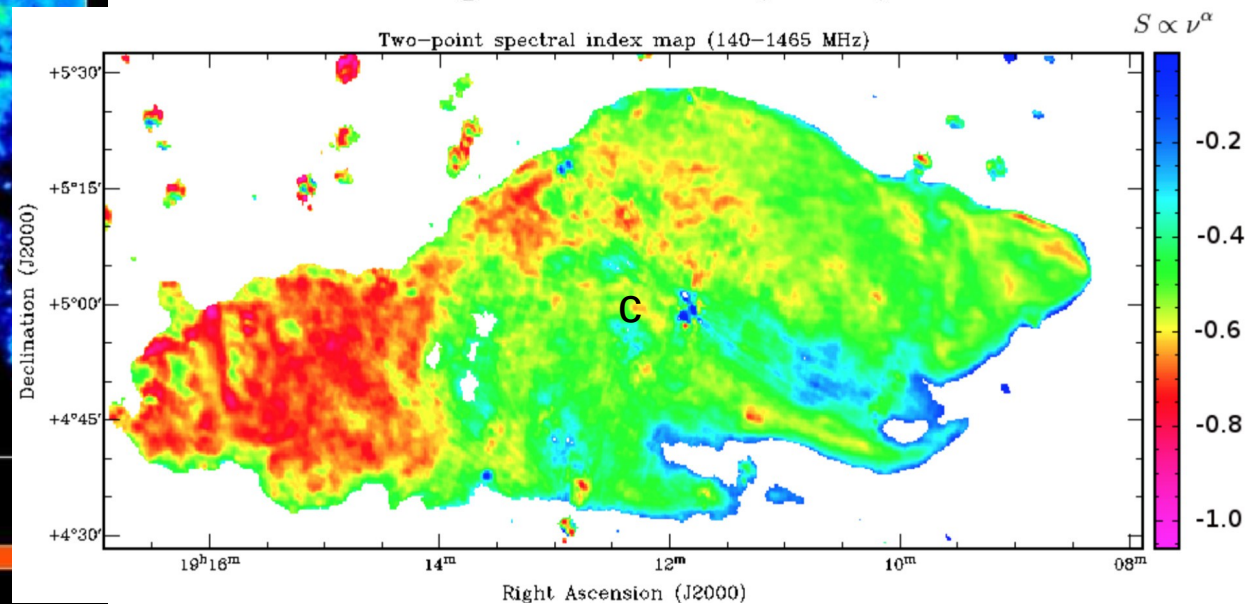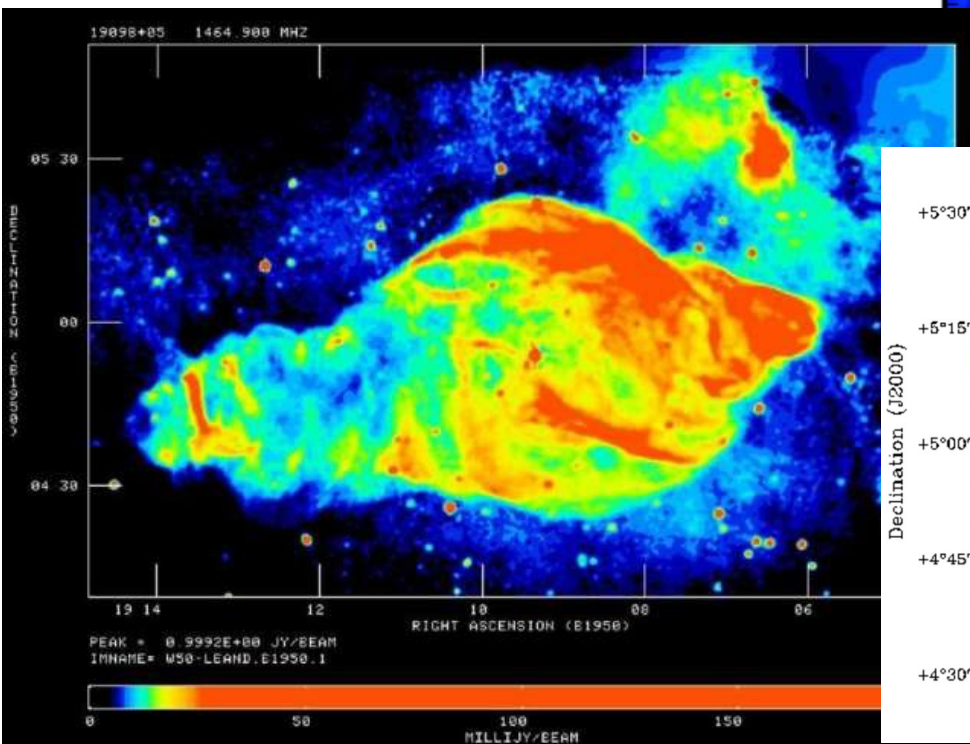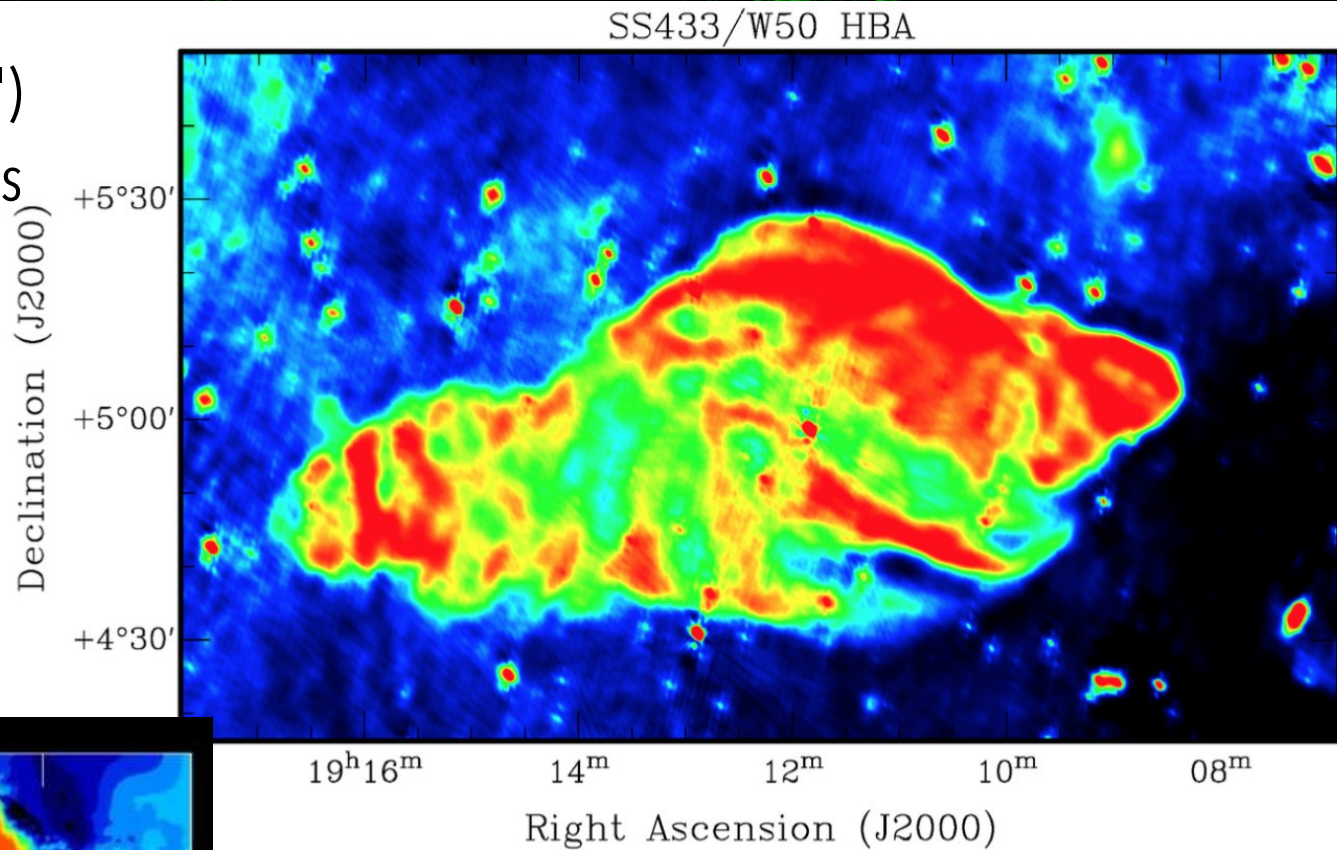
First discovered microquasar*.

- Eclipsing binary. Primary: most likely a 16±4 M$_\odot$ BH, at the center of the W50 SNR.
  The spectrum of the donor star suggests that it is a late A-type star (3 to 30 M$_\odot$)

- 433rd in the catalog of stars with strong emission lines by Sanduleak & Stephenson (1977).

- At 5.5 kpc in the galactic plane

- The material in the jets travels at 0.26c

- Orbital period of 13.1 days.

- Jets and disk precess around an axis inclined about 80° to the LoS to SS 433. The angle between the jets and the axis is around 20°, and the precessional period is around 162.5 days. As they impact the surrounding W50 SNR clouds, they distort it into an elongated shape.

* credit has been given only after the discovery/interpretation of the first microquasar

The spectrum of SS 433 is affected not just by Doppler shift but also by relativity: when the effects of the Doppler shift are subtracted, there is a residual redshift which corresponds to a velocity of about 12,000 km/s. This does not represent an actual velocity of the system away from the Earth; rather, it is due to time dilation, which makes moving clocks appear to stationary observers to be ticking more slowly. In this case, the relativistically moving excited atoms in the jets appear to vibrate more slowly and their radiation thus appears red-shifted.

The donor: blu-shifted, rest and red-shifted lines

SS 433
1979 March 20
z = (0.090, −0.019)

Margon et al. 1979
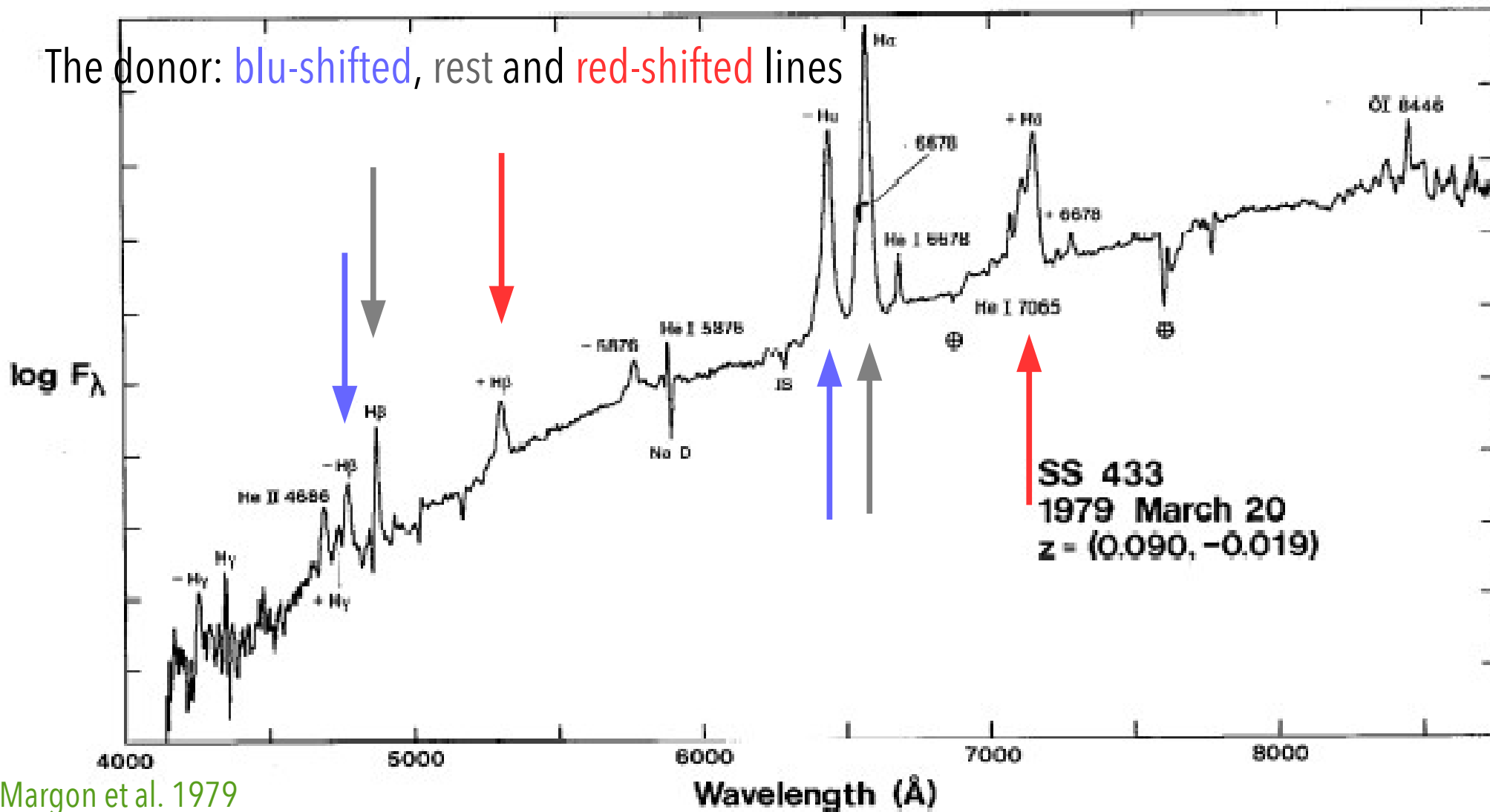
The donor: changing the red/blue -shift of the lines as the orbit develops
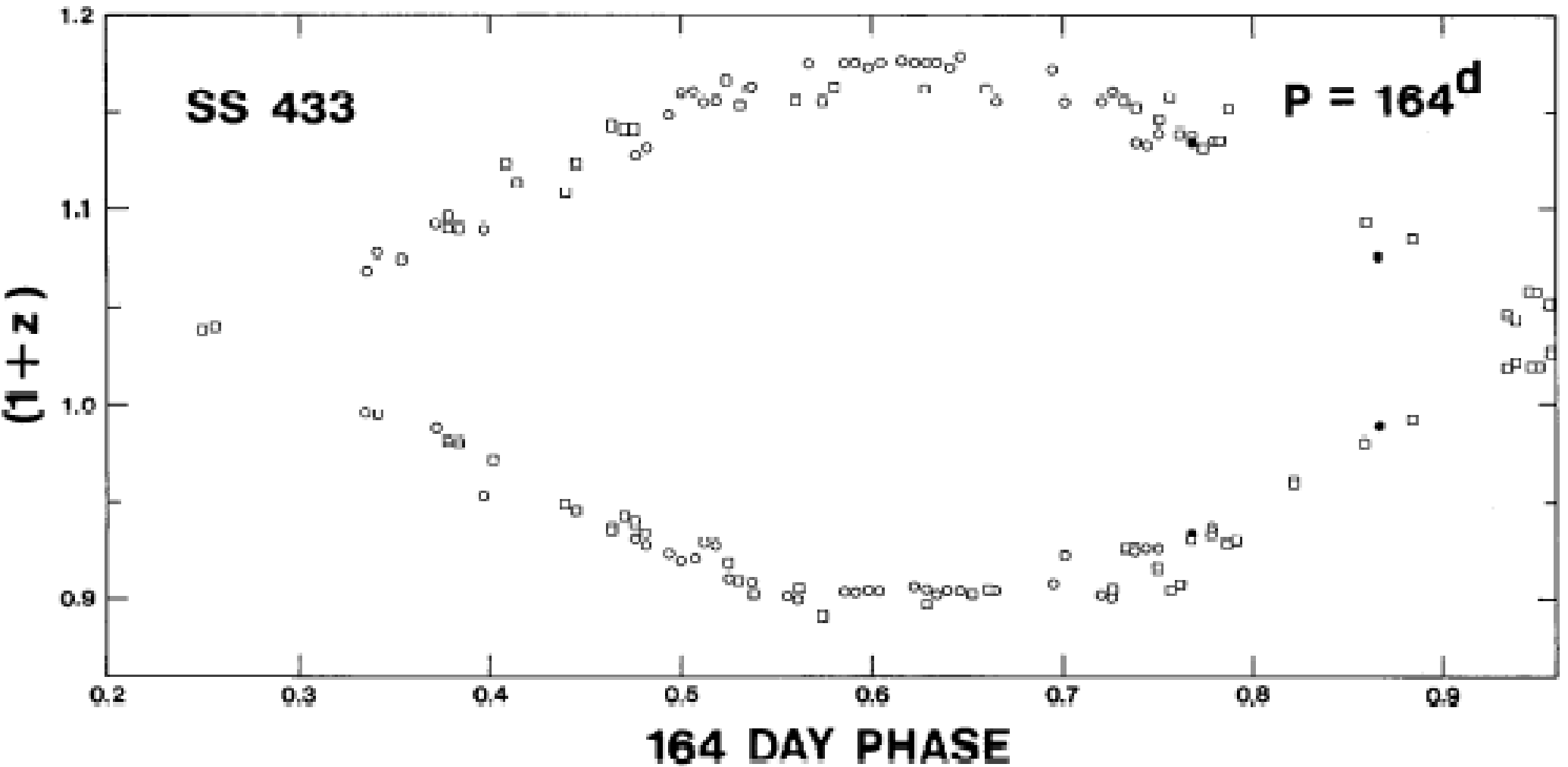
Milliarcsecond scale monitoring: https://www.youtube.com/watch?v=iz5UbKmvyik

2004, VLBA for 42 consecutive days: (see also https://www.nrao.edu/pr/2004/ss433/)

jets are sometimes impacting material shortly after being created and thus brightening.


Arcsecond scale structure
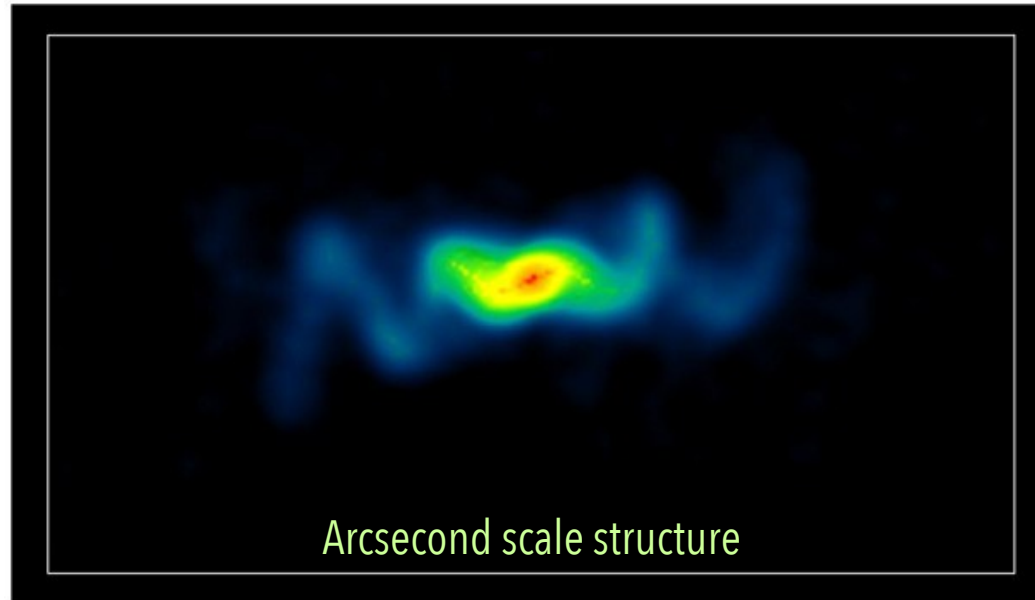
Jet precession observed at X-ray?, optical? & radio wavelengths, well fitted with a kinematic model

Two opposite collimated jets (<20 deg) come out from the compact object, preceding around a 79 deg axis, with a **period of 164 d**

Transient X-ray jets, do not have any correlation with the radio core activity

(X-rays are not the tail of the synchrotron spectrum)

The geometrical model

9 R$_\odot$

11°

84°
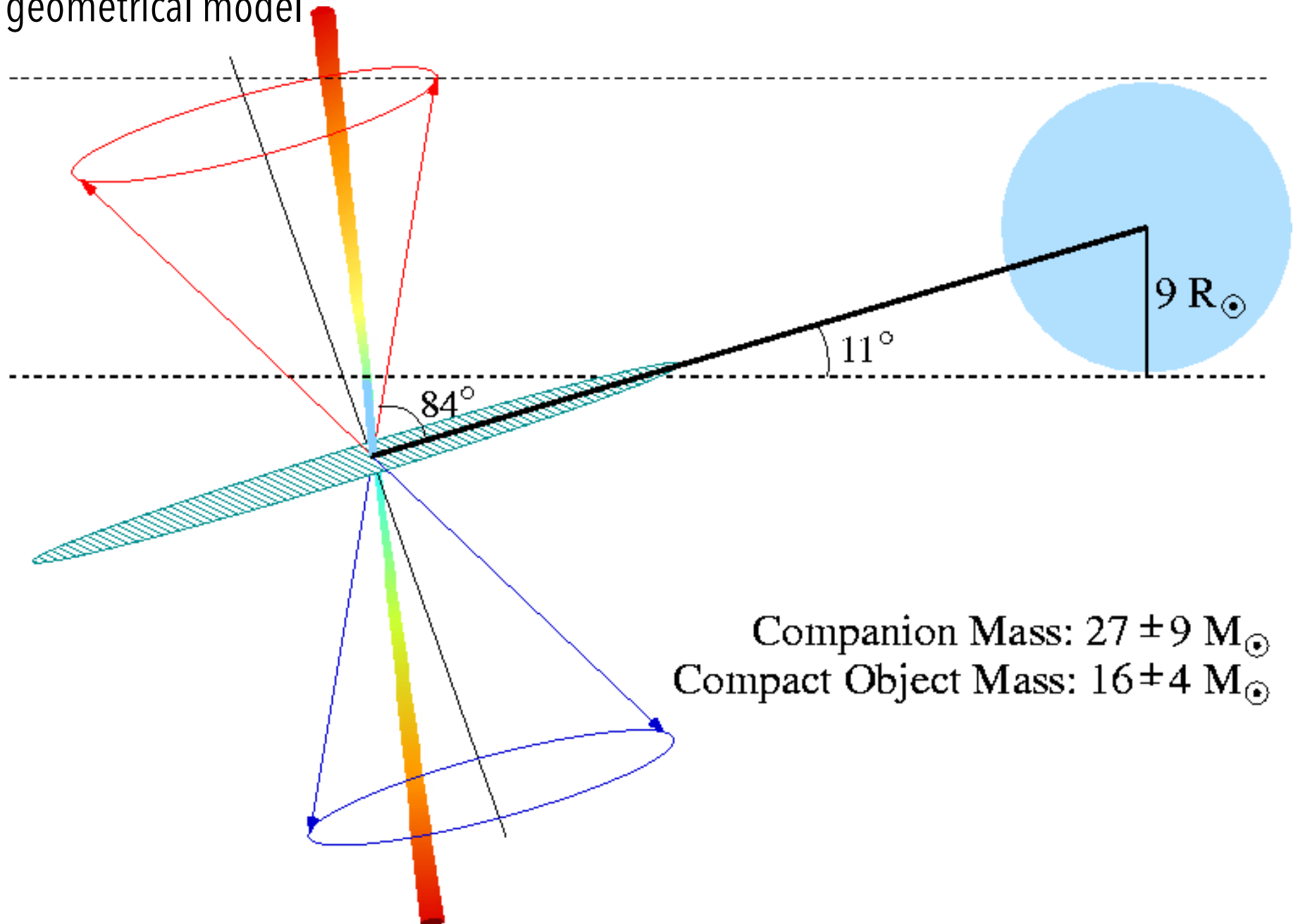
Companion Mass: 27 ±9 M$_\odot$
Compact Object Mass: 16 ±4 M$_\odot$

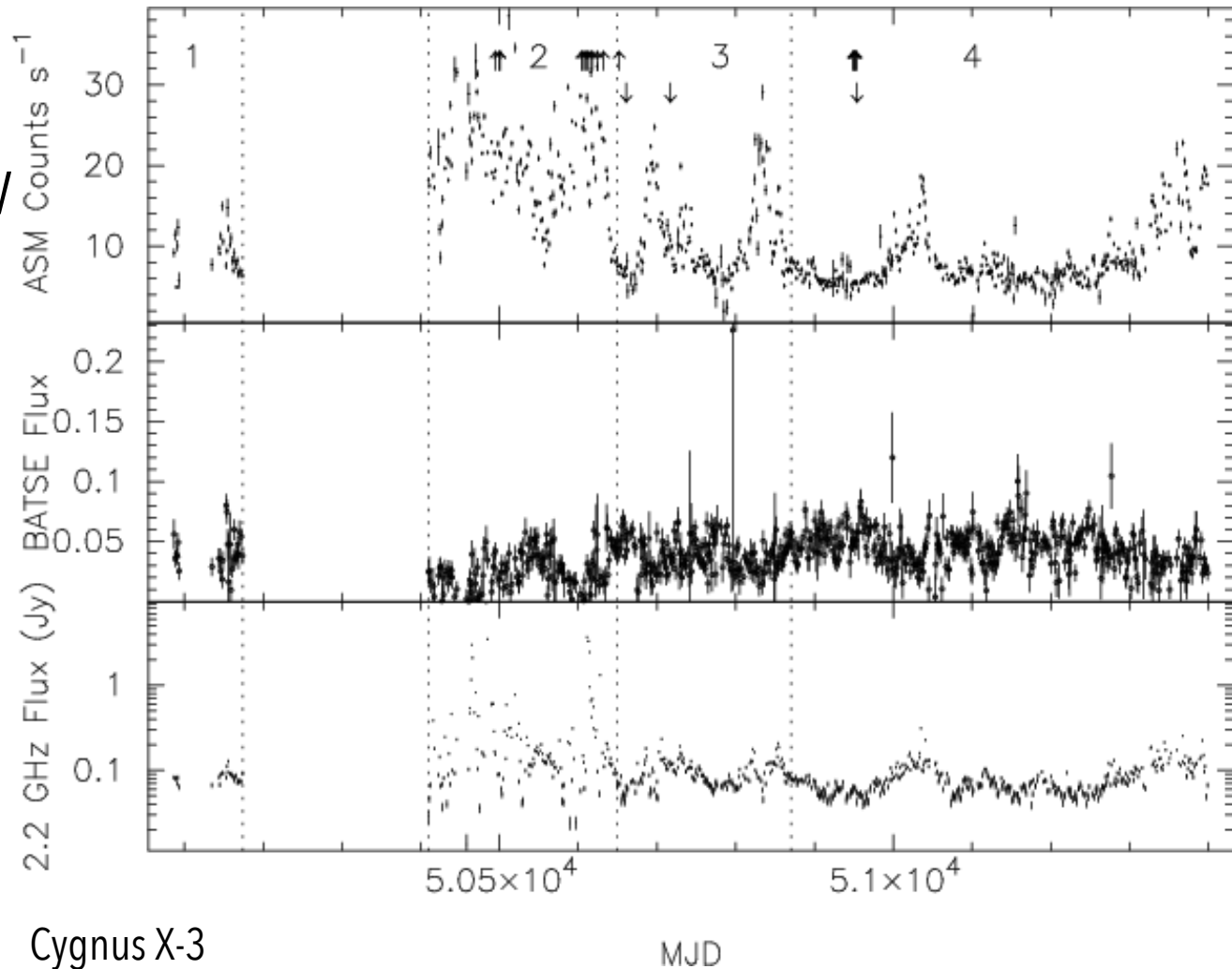Marshall et al. 2004 press release (see also Marshall et al. 2013)

HMXRB, NS, the strongest X-ray source (obscured, then not as bright as Cyg X-1)

Orbital period: 4.8 h

Distance: 7.2 kpc

Detected out to 100-1000 TeV

Mild variability with period of 4.8h, plus outbursts (even 1000x in the radio)

Cygnus X-3
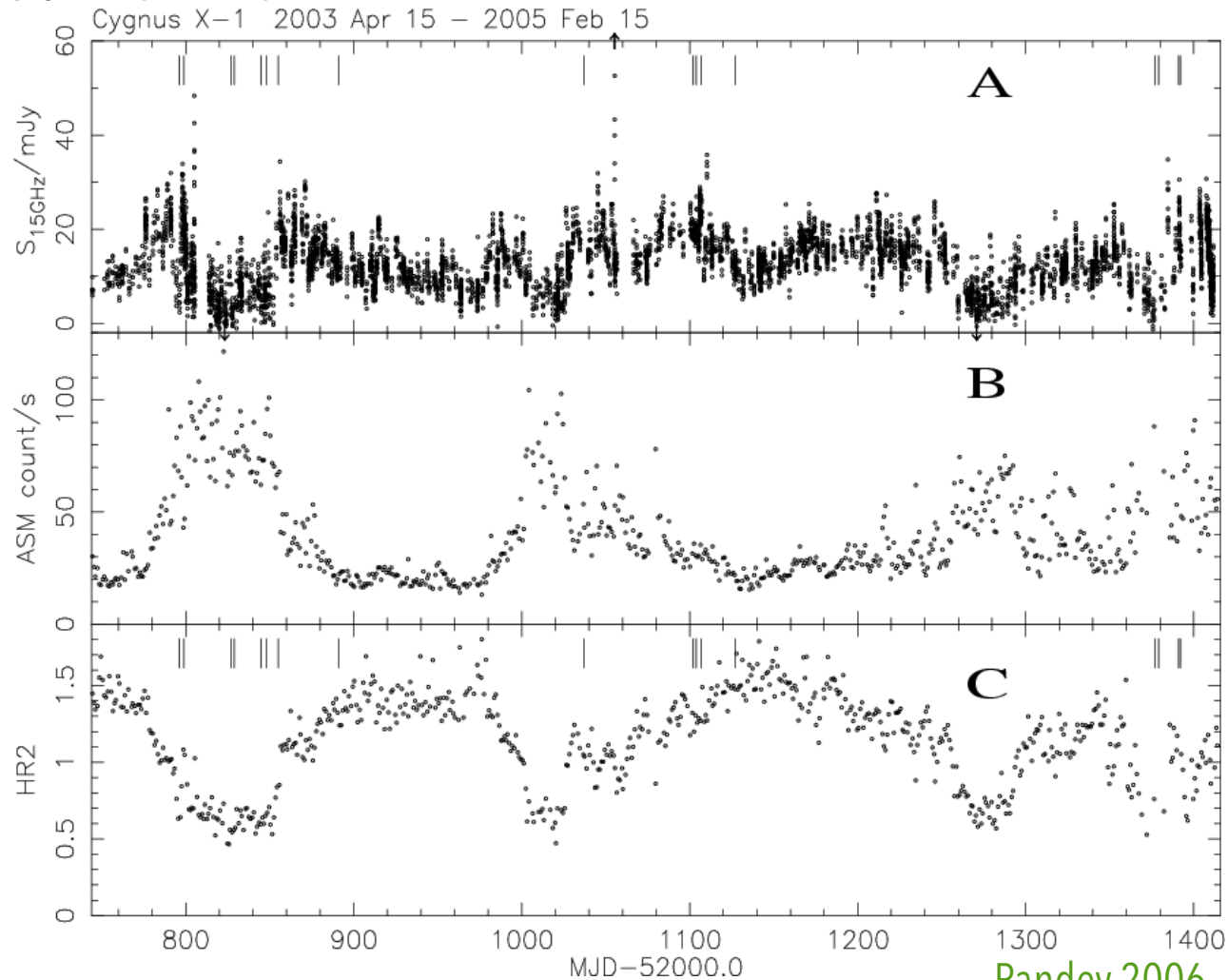Choudhury et al. (2002)

HMXRB (HDE 226868, ~ 30 M☉), BH (16 M☉), the brightest persistent X-ray source

Orbital period: 5.6 days

Distance: 1.9 kpc

Separation 0.2 AU, orbit inclination $40 \pm 10°$

Uncertain spin rate (790 rps)

Pandey 2006

Microquasars: Cyg X-1
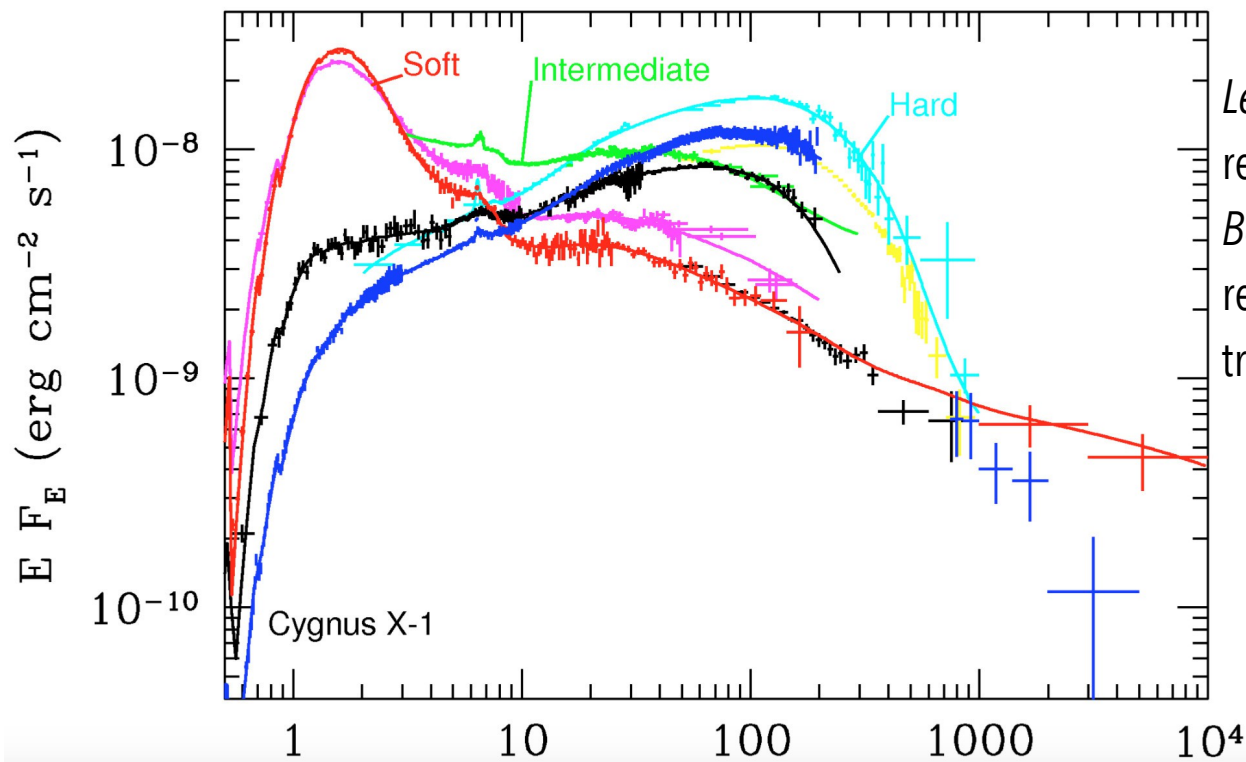
Left: examples of variability of the central component related to the changes in the inner structure.

Below: the radio jet visible on the small scale is responsible for the egg-shaped diffuse emission tracing the interaction with the ambient medium

From Nature 436, 819-821 (11 August 2005)

Vrtilek 2008
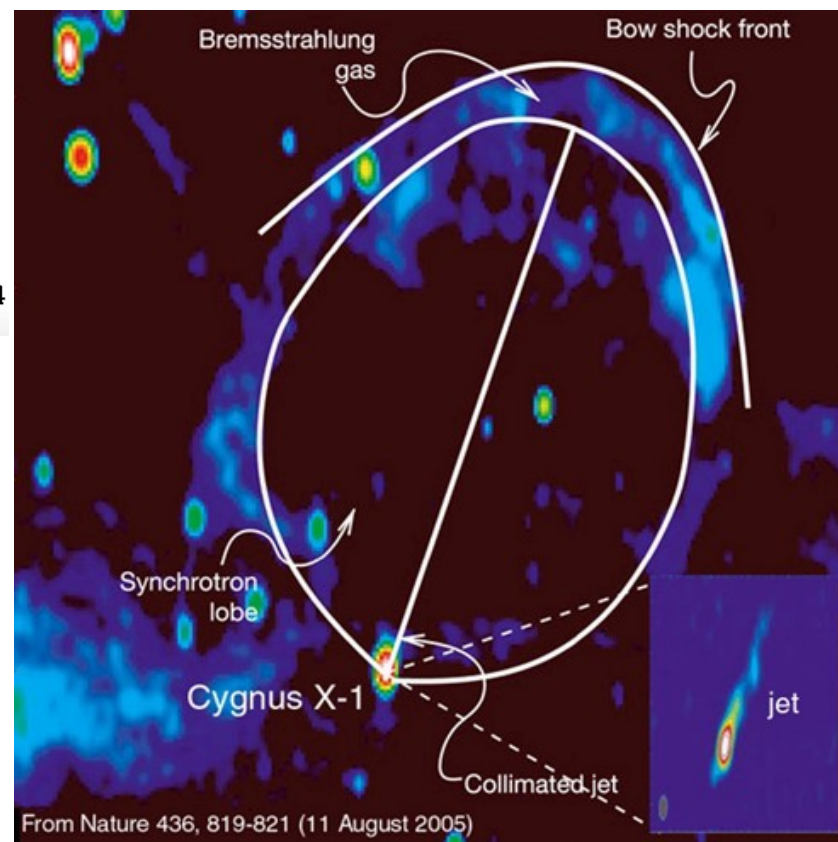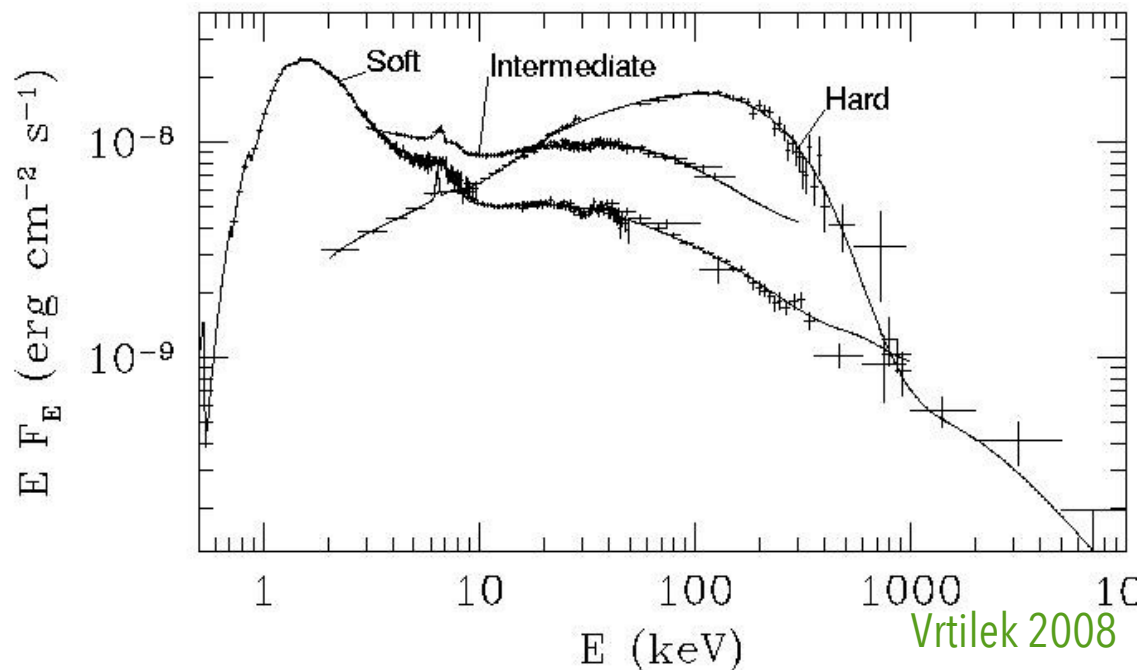
A dozen of X-ray variability schemes:
a few examples.

X-rays are common and drive the
Classification

Hardness ratio (HR1 vs HR2)
& Counts .vs. time
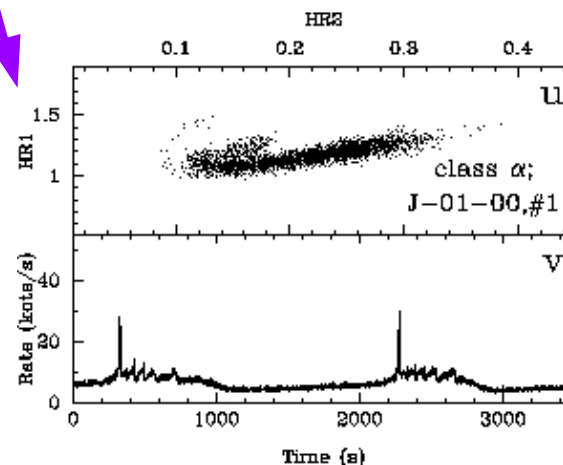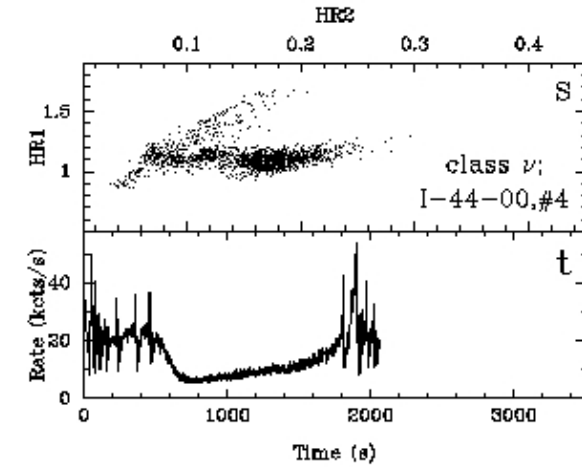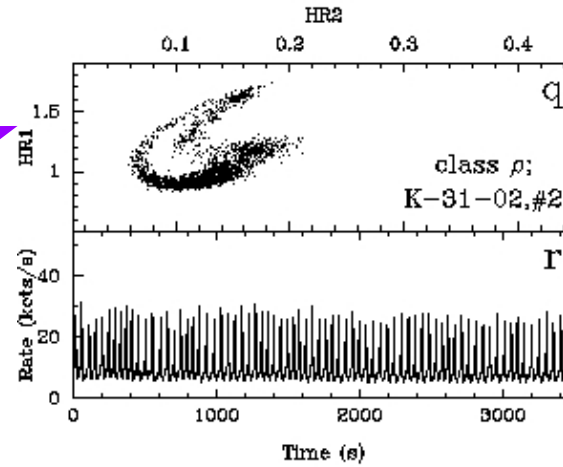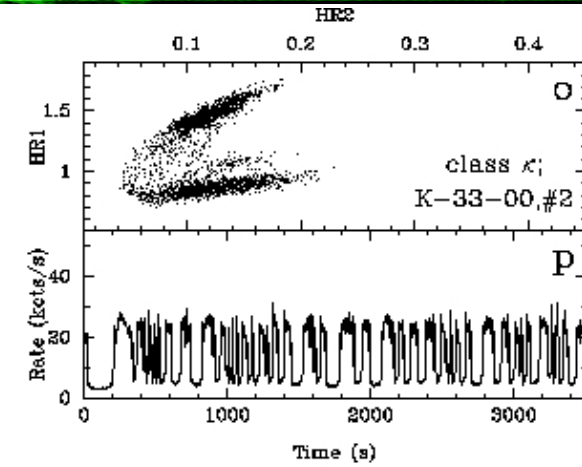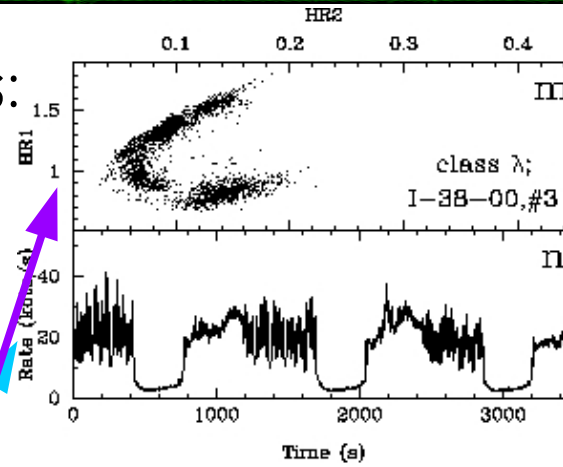
Summary (1):

➢ About 15% of XRBs have radio emission (variability!) related to jet activity

  Observations are often triggered by flaring episodes. Quiescent state much weaker

  May be that the fraction of XRBs increases if the flux density limit is lowered.

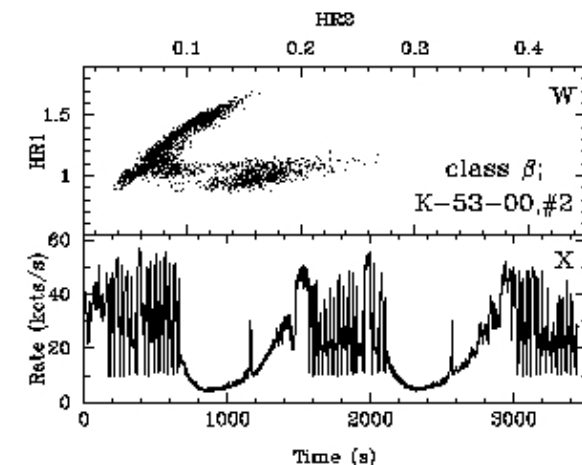➢ High resolution images reveal fast motion & evolution of plasmoids, often moving superluminally in jets, visible on both sides of the compact object position

➢ No hot-spots

  Combination of jet speed and ambient density

➢ No lobes (may be in SS443)

  Adiabatic expansion kills the radio emission (unless going at very low frequencies!)

➢ Energetics $\sim 10^{37}$ erg s^{-1}, a fraction of the Eddington luminosity

➢ Tight connection with X-ray emission

Summary (2):

- Radio jets appear when X-ray emission decays and are visible during disk replenishment
- Delay of peaks (decays) in the radio light curves consistent with adiabatic expansion of a bubble of relativistic plasma
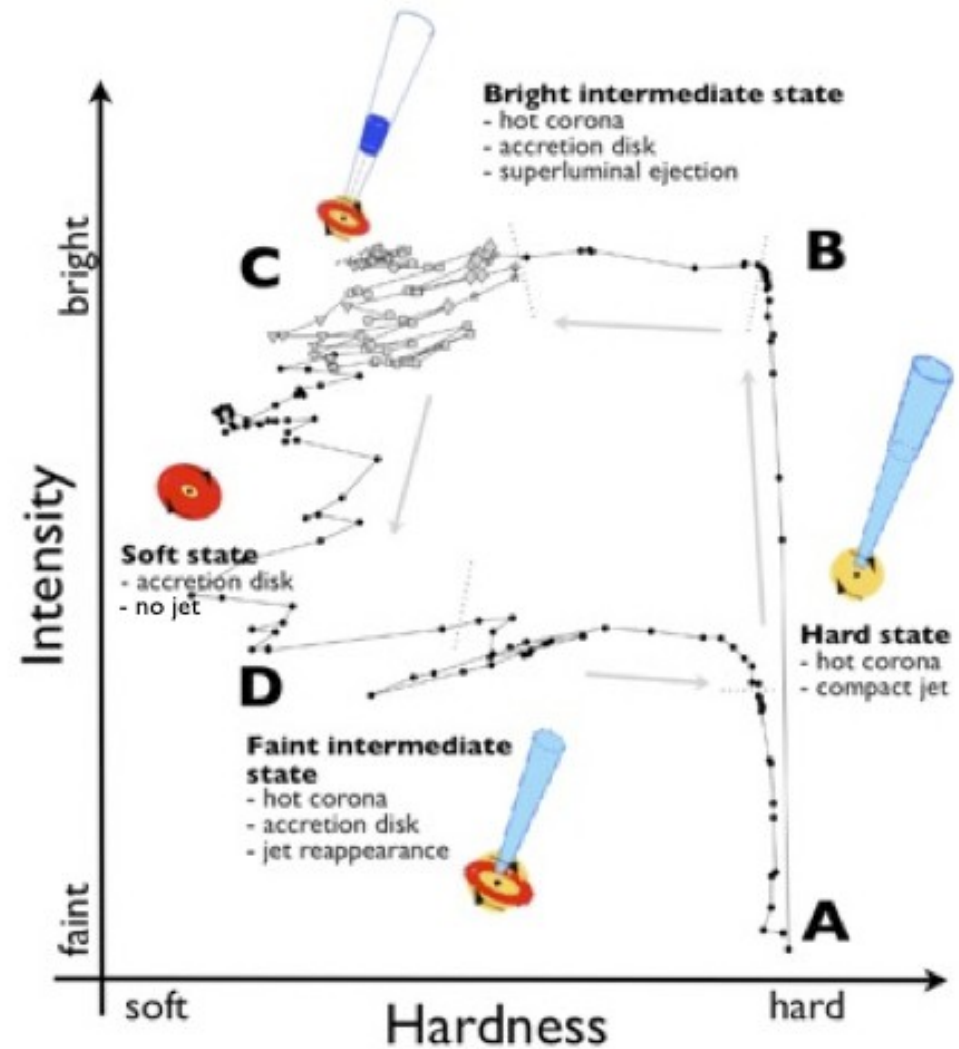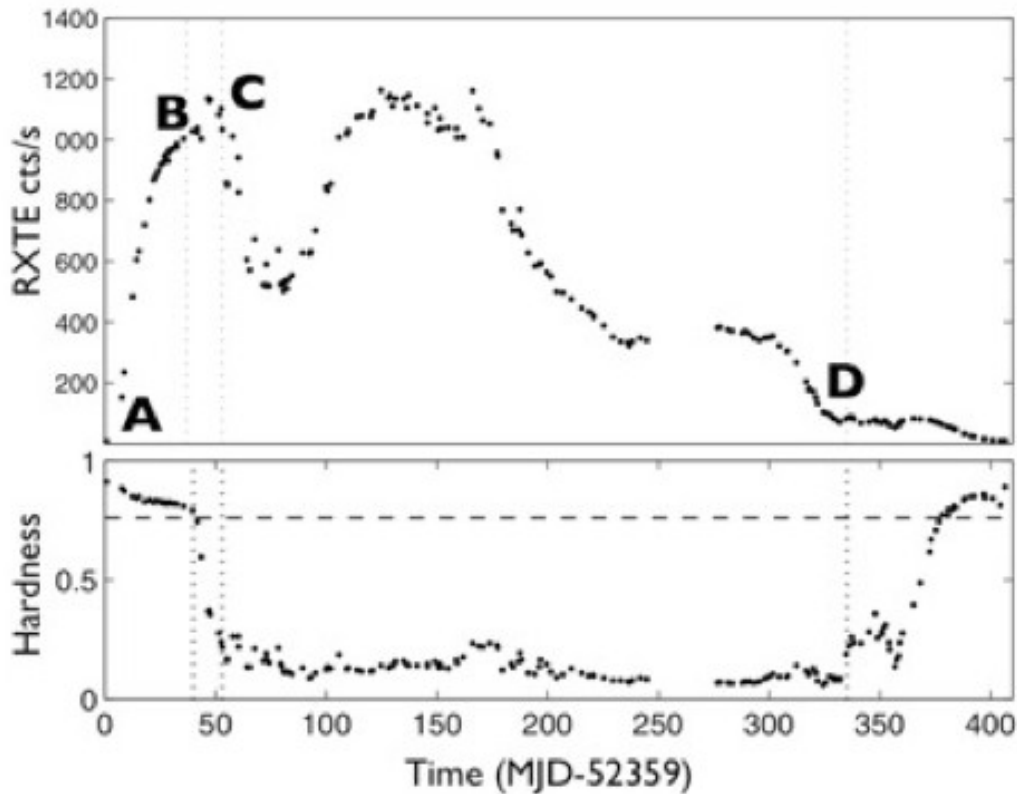
Disc-corona System

accretion
rate

(Chris Done et al, 2007)
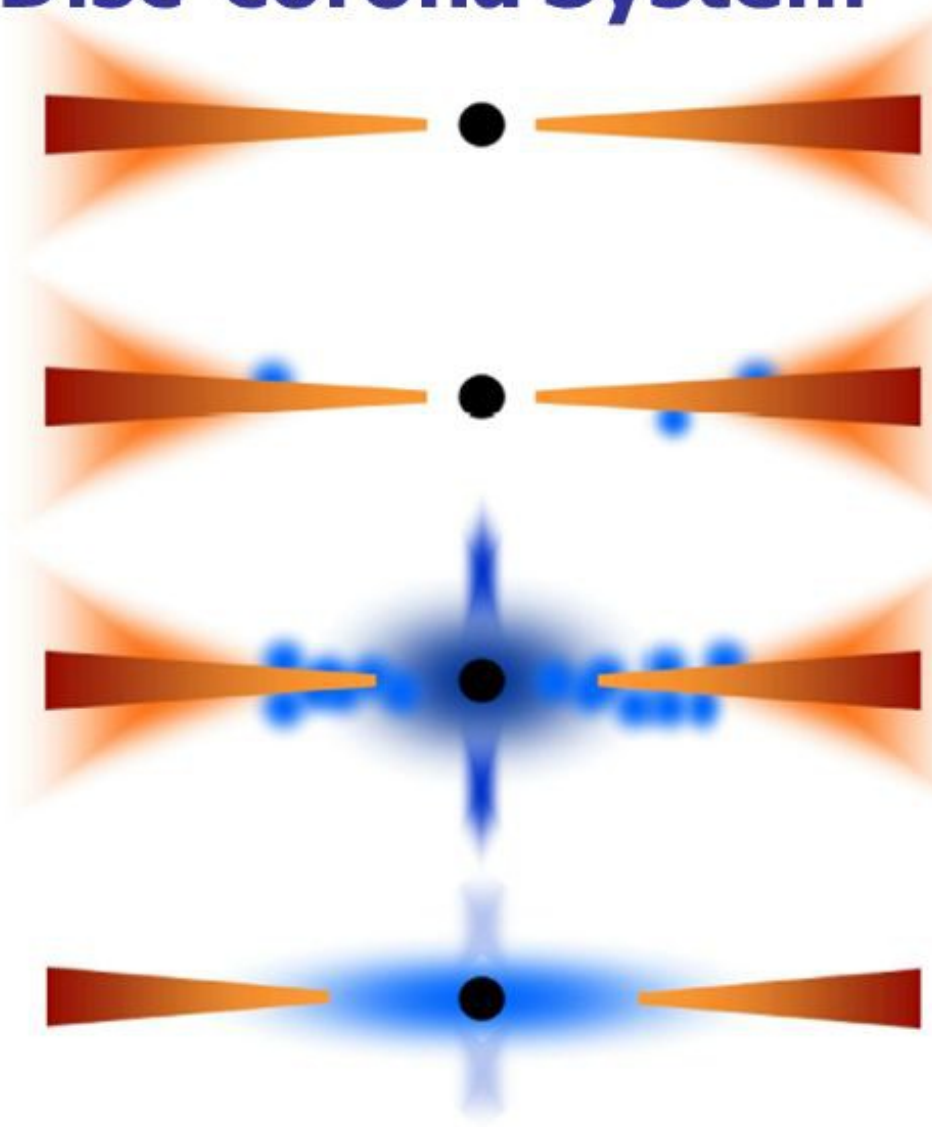
high/
soft
state

low/
hard
state

Rees (1984): the characteristic temperature of a black body in the last stable orbit in the accretion disk is:

$$T \sim 2 \times 10^{7} \ M^{-1/4} \quad \text{(T,M of the black hole)}$$

(i.e. the more massive is the BH the colder is the accretion disk around it => in AGN the emission is at visible and UV wavelenghts, in the galactic sources the emission is at X and gamma wavelengths)

SS433: peculiar object, its accretion disk emits at optical frequencies.
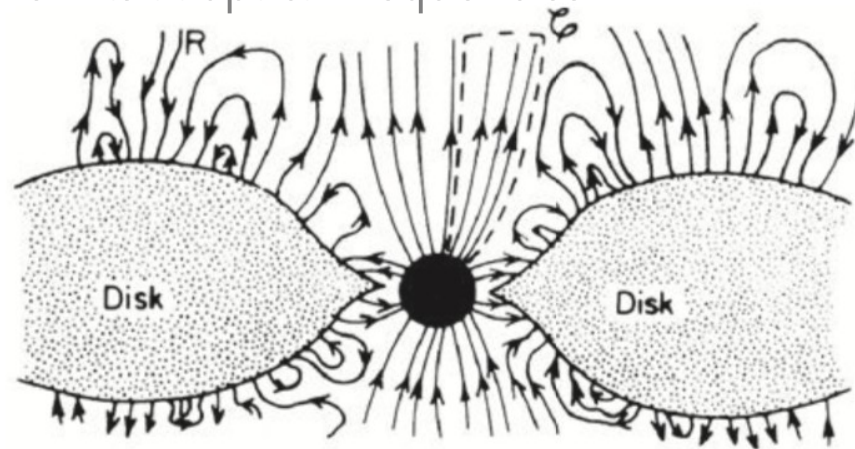
A possible configuration for the magnetic field distribution about a black hole which is surrounded by a thick accretion disc. The magnetic field lines are linked to both the accretion disc and the surrounding medium (Thorne *et al.*, 1986).

https://vimeo.com/332582739
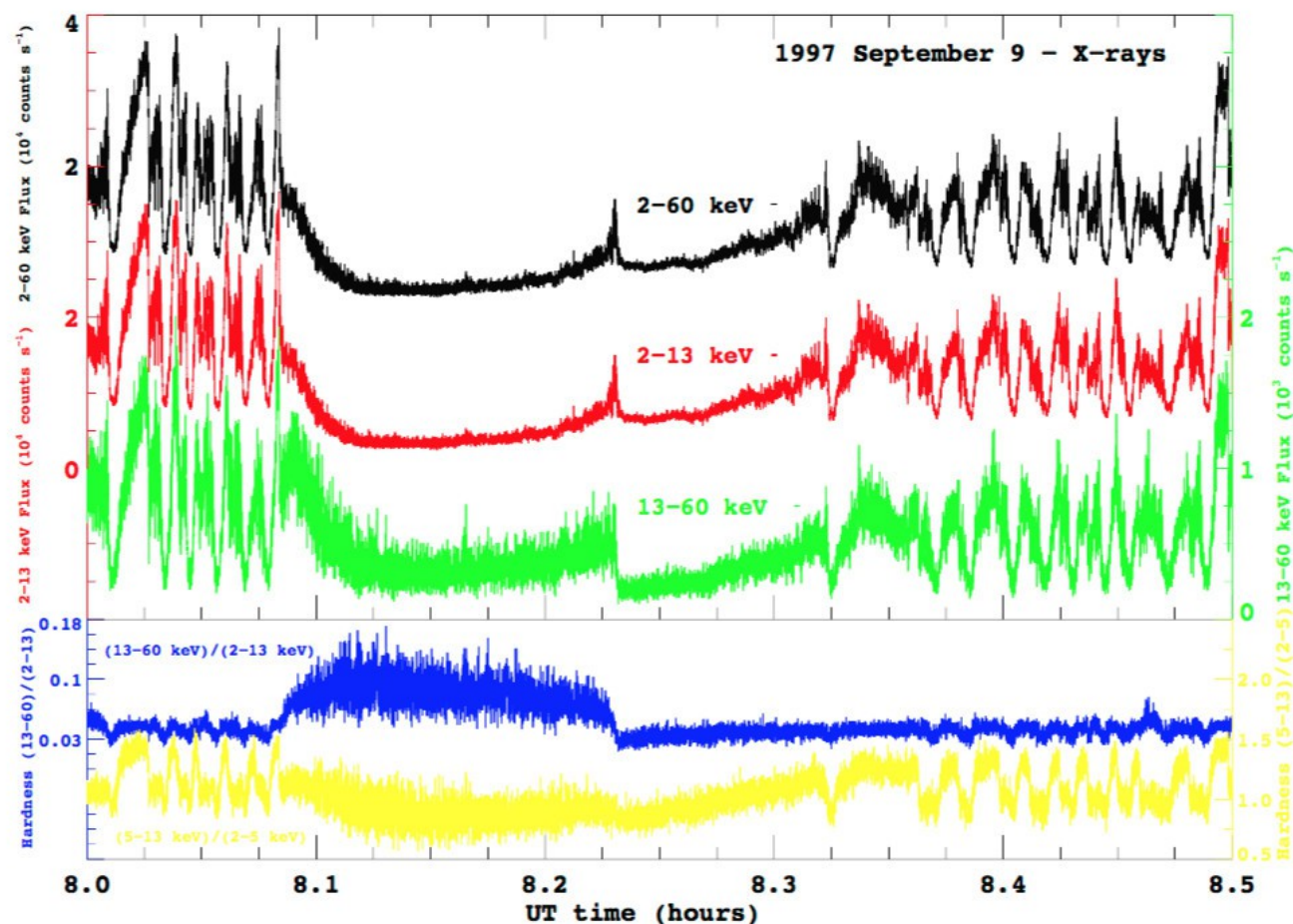
Figure 3: Same observations as above, with only X-ray observations, and enlarged on the UT interval [8.0-8.5] hours. From top to bottom: 2-60 keV, 2-13 keV and 13-60 keV X-ray flux; hardness ratio $\frac{13-60keV}{2-13keV}$ and $\frac{5-13keV}{2-5keV}$. These observations suggest that it is a part of the corona which is ejected at the time of the X-ray spike (Chaty, 1998).

09B.   Fast Radio Bursts (FRBs)

– Rane & Lorimer, JAA 2017, 38:55 (DOI 10.1007/s12036-017-9478-1)
"Fast Radio Bursts"

– Cordes & Chatterjee, ARAA, 2019, 57, 417-465
"Fast Radio Bursts: An Extragalactic Enigma"

– Metzger, Margalit & Sironi: 2019, MNRAS 485, 4091-4016
"Fast radio bursts as synchrotron maser emission from decelerating relativistic blast waves"

– Clay Fellowship Lecture on Fast Radio Bursts
   https://www.youtube.com/watch?v=aagnzOpHM90

DETECTION diagrams (DM effect on time of arrival)

a FRB 010724 **b** FRB 110220 **c** FRB 121102
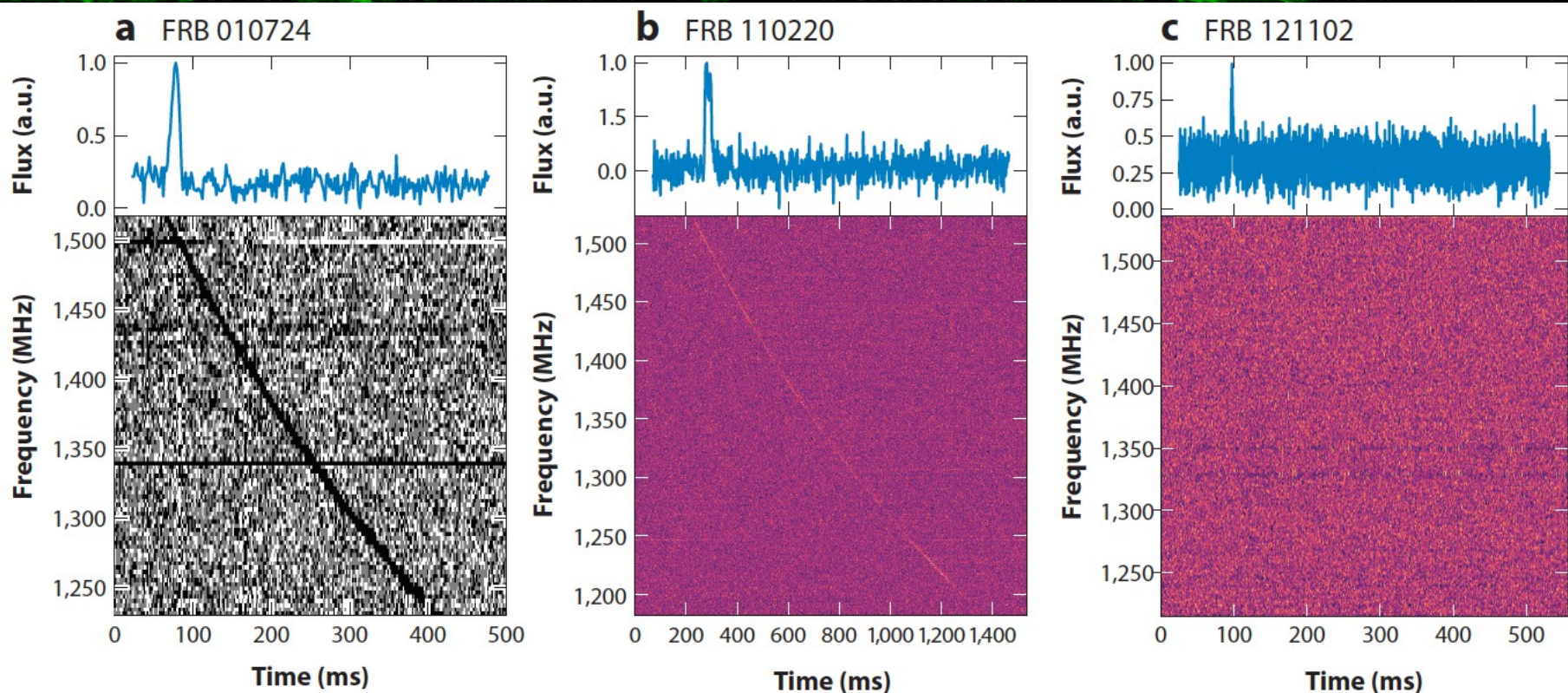
Figure 1

FRB dynamic spectra. In each case, the lower panel shows the sweep of the burst across the time–frequency plane, and the upper panel shows the total pulse intensity after removing the best-fit quadratic dispersion sweep and frequency-averaging across the band. Time and frequency resolutions vary, depending on the instrument. (*a*) FRB 010724, the first-reported fast radio burst with DM = 375 pc cm^{-3}. (*b*) FRB 110220, detected at Parkes with DM = 944.4 pc cm^{-3}, leading to the realization that FRBs were most likely astrophysical in nature. (*c*) The original detection of FRB 121102 at Arecibo, the first reported non-Parkes FRB, with DM = 557.4 pc cm^{-3}. Panels use data taken with permission from (*a*) Lorimer et al. (2007), (*b*) Thornton et al. (2013), and (*c*) Spitler et al. (2014). Abbreviations: DM, dispersion measure; FRB, fast radio burst.

➢ Isolated pulses

➢ Behave like pulsars (i.e. DM!)

➢ FRB 010724 first detected by (Narkevic) Lorimer + Science, Volume 318, Issue 5851, pp. 777- (2007).

Figure 2

FRB dynamic spectra. In each case, the lower panel shows the burst on the time–frequency plane after removing the best-fit quadratic pulse dispersion sweep, and the upper panel shows the dedispersed pulse total intensity after frequency-averaging across the band. Time and frequency resolutions vary, depending on the instrument. (*a*) FRB 170827, detected at UTMOST with DM = 899 pc cm^{-3}. Voltage capture was triggered after real-time detection, and coherent dedispersion reveals fine structure in the burst. (*b*) FRB 170922, detected at UTMOST with DM = 1,111 pc cm^{-3} and with very significant pulse scattering. (*c*) FRB 180110, a bright burst detected with ASKAP in fly's-eye mode with DM = 716 pc cm^{-3}. Panels use data taken with permission from (*a*) Farah et al. (2018), (*b*) Farah et al. (2017), and (*c*) Shannon et al. (2018). Abbreviations: ASKAP, Australian Square Kilometre Array Pathfinder; DM, dispersion measure; FRB, fast radio burst; UTMOST, the updated Molonglo Observatory Synthesis Telescope.
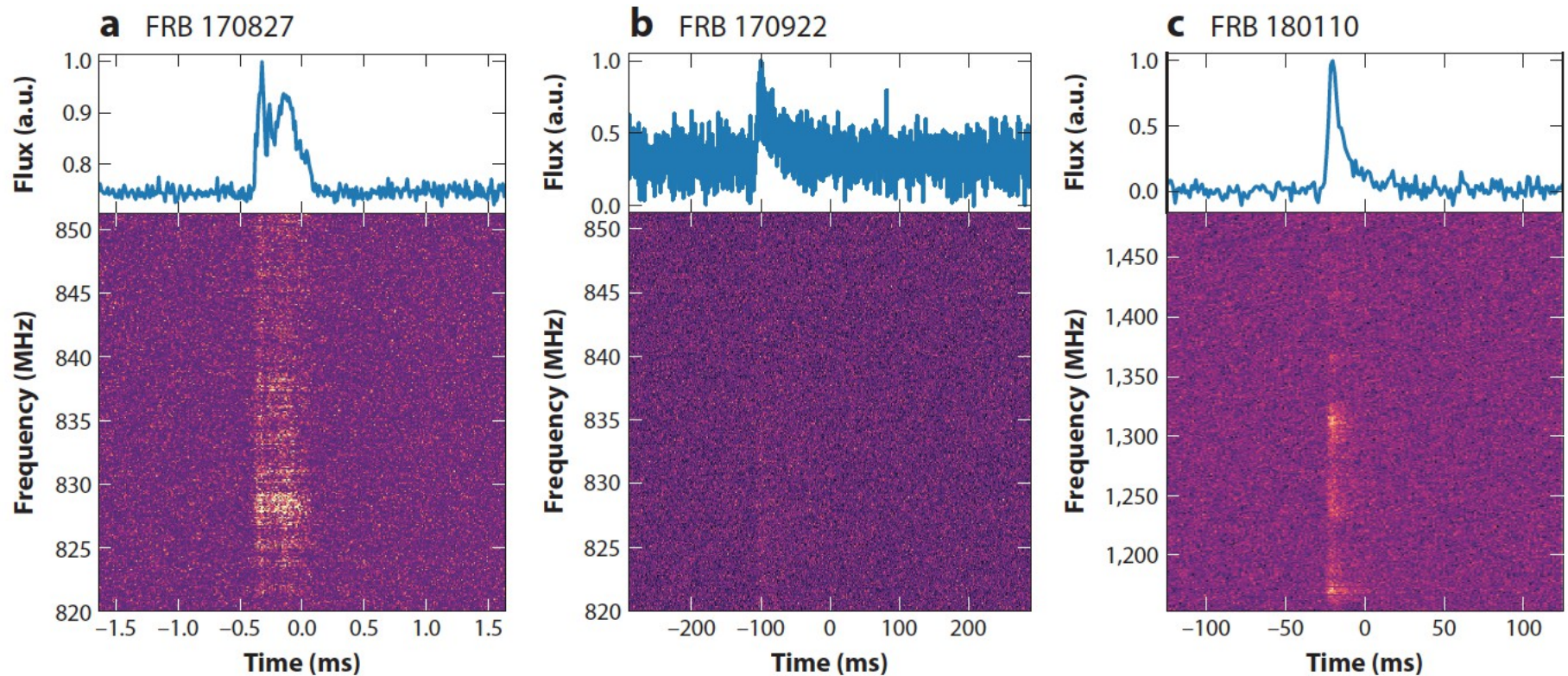
➢ Pulse profile
➢ Duration & scattering?
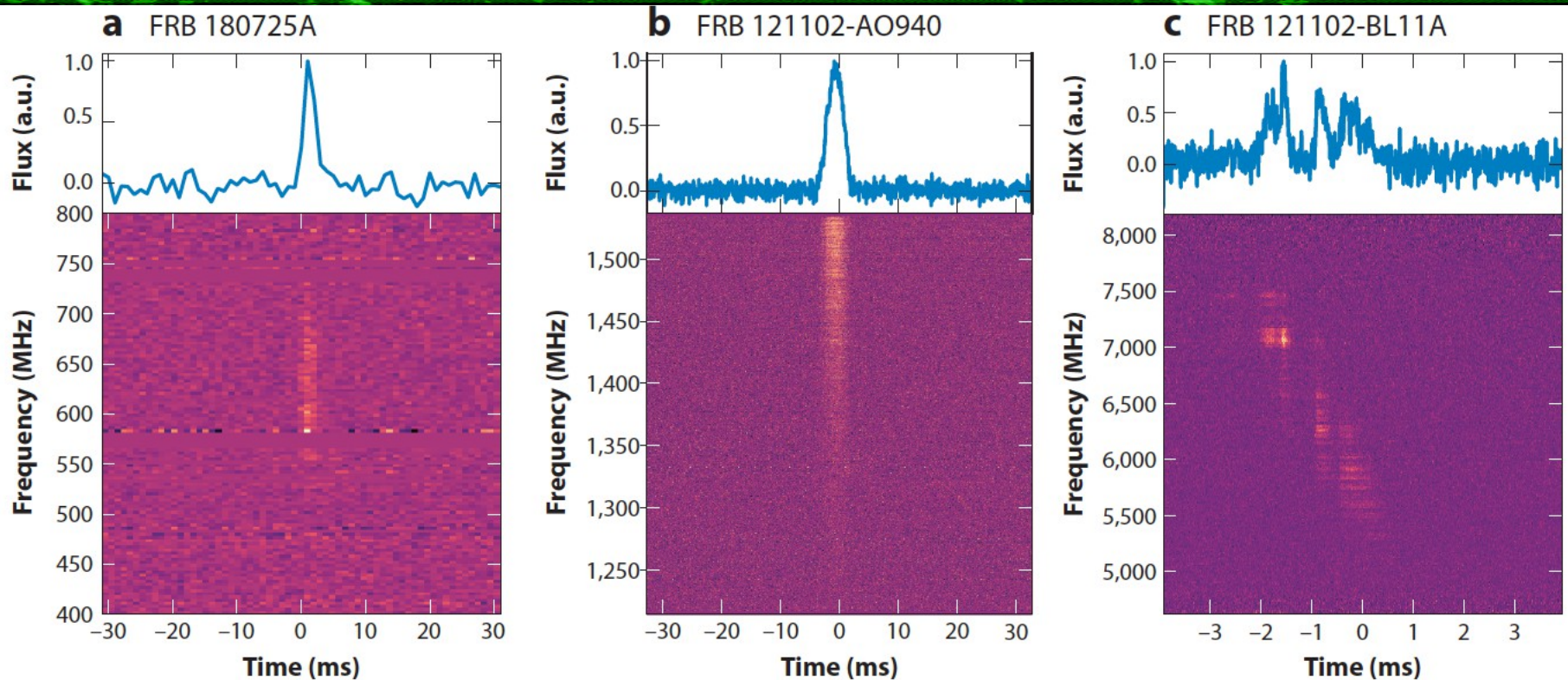
Figure 3

FRB dynamic spectra. As in **Figure 2**, the lower panel shows the burst on the time–frequency plane after removing the best-fit quadratic pulse dispersion sweep, and the upper panel shows the dedispersed pulse total intensity after frequency-averaging across the band. Time and frequency resolutions vary, depending on the instrument. (*a*) FRB 180725A, the first FRB detected at CHIME and at frequencies down to 550 MHz with DM = 716.6 pc cm^{-3}. (*b*) One of the first and brightest redetections of FRB 121102 at Arecibo at 1.2–1.6 GHz. (*c*) Another detection of FRB 121102 at the Green Bank Telescope but at 4–8 GHz. Precise localization enabled high-frequency observations, and the known DM allowed coherent dedispersion, revealing extensive pulse structure at these higher frequencies. Panels use data taken with permission from (*a*) CHIME/FRB Collab. et al. (2019a), (*b*) Spitler et al. (2016), and (*c*) Gajjar et al. (2018). Abbreviations: CHIME, Canadian Hydrogen Intensity Mapping Experiment; DM, dispersion measure; FRB, fast radio burst.

- ➤ Broad band spectra
- ➤ Unusual frequency coverage (partial coverage)
- ➤ C may suggest a pulse profile complex origin (Linear size ? Different site? Opacity? What else?).

Table 1 Large-scale surveys at 1.4 GHz that constrain FRB population estimates

Telescope/Survey	$\mathcal{F}_{min}$ (Jy ms)	$\Omega_s T$ (deg² h)	N_{frb}	Γ_{frb}[a] (sky⁻¹ day⁻¹)	References
Parkes/all[b]	2	4,400	19	$1.7^{+1.5}_{-0.9} \times 10^3$	Bhandari et al. (2018)
Parkes/HTRU(h)	2	1,549	9	$2.5^{+3.2}_{-1.6} \times 10^3$	Thornton et al. (2013), Champion et al. (2016)
Parkes/HTRU(m)	2	694	0	$\lesssim 1.4 \times 10^3$	Petroff et al. (2014)
Parkes/SUPERB	2	1,621	5	$1.7^{+1.5}_{-0.9} \times 10^3$	Bhandari et al. (2018), Keane et al. (2018)
Arecibo/PALFA[c]					
Outer Galaxy					Spitler et al. (2014)
Main beam	0.065	6.2	1	$1.6^{+6}_{-1.5} \times 10^5$	FRB 121102
Sidelobes	0.350	29.7	1	$3.1^{+12}_{-3.1} \times 10^4$	FRB 121102
Outer+inner Galaxy					Scholz et al. (2016)
Main beam	0.057	19.5	1	$5.1^{+17.8}_{-4.8} \times 10^4$	FRB 121102
Sidelobes	0.300	93	1	$1.1^{+3.7}_{-1.0} \times 10^4$	FRB 121102
Outer+inner Galaxy					Patel et al. (2018)
Main beam	0.044	12.7	1	$7.8^{+25.6}_{-7.6} \times 10^4$	FRB 141113
Sidelobes	0.239	60	1	$1.6^{+7.5}_{-1.6} \times 10^4$	FRB 141113
ASKAP/Fly's Eye	29.2	5.1×10^5	20	37 ± 8	Shannon et al. (2018)

[a]The mean FRB rate is $4\pi \times (180/\pi)^2 \times 24 \times N_{frb}/\Omega_s T$, but the rates given account for fluence completeness (Keane & Petroff 2015).
[b]This line includes all Parkes observations reported by Bhandari et al. (2018), their table 5, which includes their FRB detections as well as 14 from the HTRU and SUPERB surveys.
[c]Arecibo values are for the subsurveys yielding FRB 121102 (Spitler et al. 2014, Scholz et al. 2016) or FRB 141113 (Patel et al. 2018). The analyses consider detection in the main lobes of the 7-beam ALFA receiver or in the sidelobes, which have a larger solid angle at lower sensitivity. The Spitler et al. analysis considers only the subsurvey of the outer Galaxy, whereas the other analyses consider the inner and outer Galaxy subsurveys together.
Abbreviations: ASKAP, Australian Square Kilometre Array Pathfinder; HTRU, High Time Resolution Universe; PALFA, pulsar survey using ALFA (Arecibo L-Band Feed Array); SUPERB, Survey for Pulsars and Extragalactic Radio Bursts.

➤ Surveys

➤ Strong dependency on frequencies

• Determine the daily rate (@ a given fluence limit)

➤ ~10^3 events sky⁻¹ day⁻¹

Table 2 Low-frequency surveys

Telescope/Survey	$\mathcal{F}_{min}$ (Jy ms)	$\Omega_s T$ (deg² h)	N_{frb}	Γ_{frb} (sky⁻¹ day⁻¹)	References
LOFAR/ARTEMIS[a] 0.145 GHz	139	3.4×10^4	0	<29	Karastergiou et al. (2015)
GBT/GBNCC[b] 0.35 GHz	1.4	580	0	$<3.6 \times 10^3$	Chawla et al. (2017)
UTMOST 0.84 GHz	11	3.8×10^4	3	$78^{+12.4}_{-0.57}$	Caleb et al. (2016)
CHIME 0.4–0.8 GHz	TBD	TBD	13	NA	CHIME/FRB Collab. et al. (2019a)

[a]Reported $\mathcal{F}_{min} = 62$ Jy $\times$ 5 ms has been scaled to $W = 1$ ms using $\mathcal{F}_{min} \propto \sqrt{W}$.
[b]Reported $\mathcal{F}_{min} = 0.63$ Jy $\times$ 5 ms has been scaled to $W = 1$ ms.
Abbreviations: ARTEMIS, Advanced Radio Transient Event Monitor and Identification System; CHIME, Canadian Hydrogen Intensity Mapping Experiment; GBT, Green Bank Telescope; GBNCC, Green Bank North Celestial Cap survey; LOFAR, Low Frequency Array; NA, not applicable; TBD, to be determined; UTMOST, the updated Molonglo Observatory Synthesis Telescope.

The effect of scattering on the pulse profile:

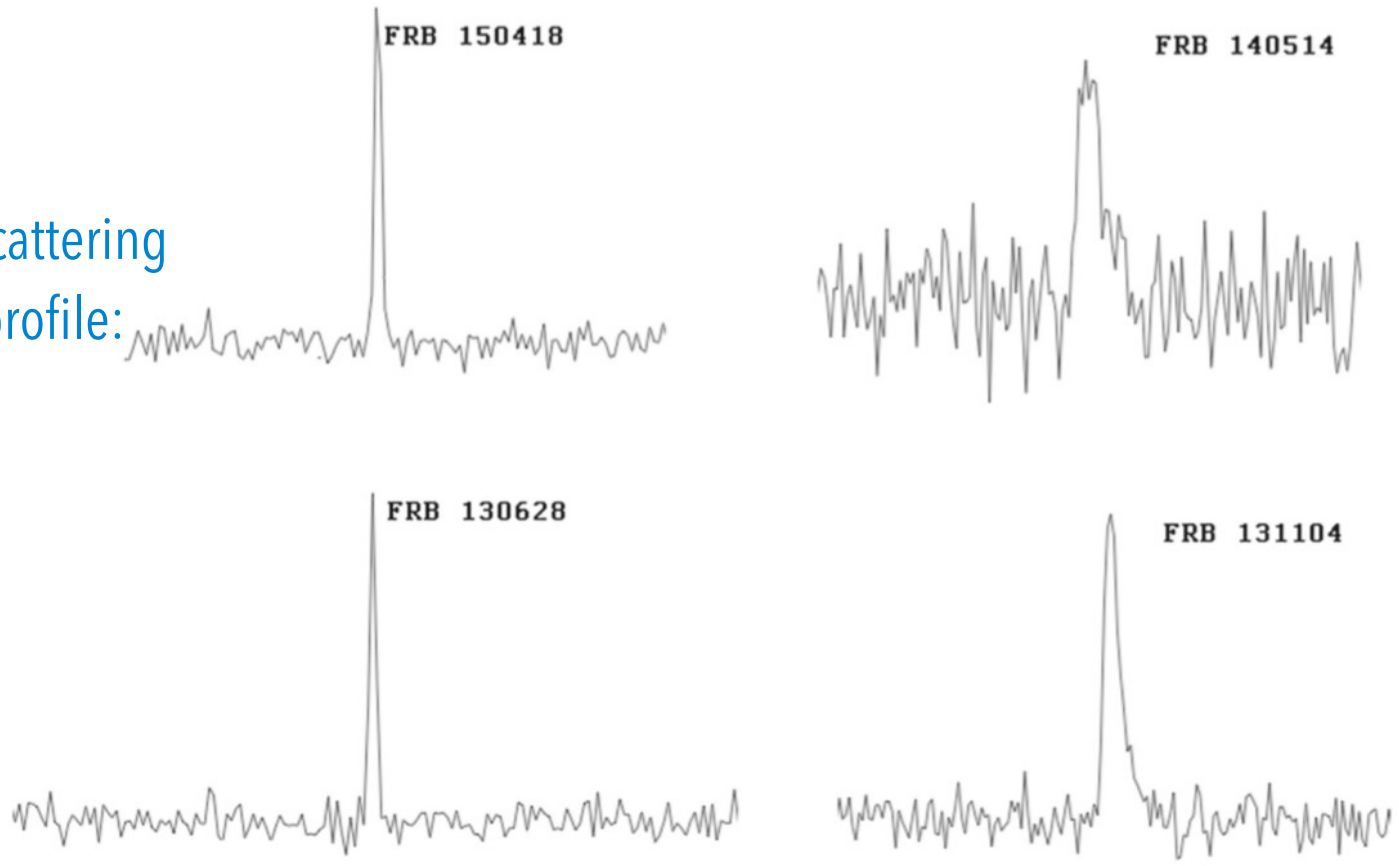The time of the (exponential) Decrease defines the Scattering time τ

Figure 3. FRBs with no scattering are shown in the *left panel* and FRBs with scattering are shown in the *right panel*. The horizontal time scale is 60 ms for each profile.

- ➤ Extragalactic origin

$$DM_{FRB} = DM_{host} + DM_{IGM} + DM_{MW} + DM_{other}$$
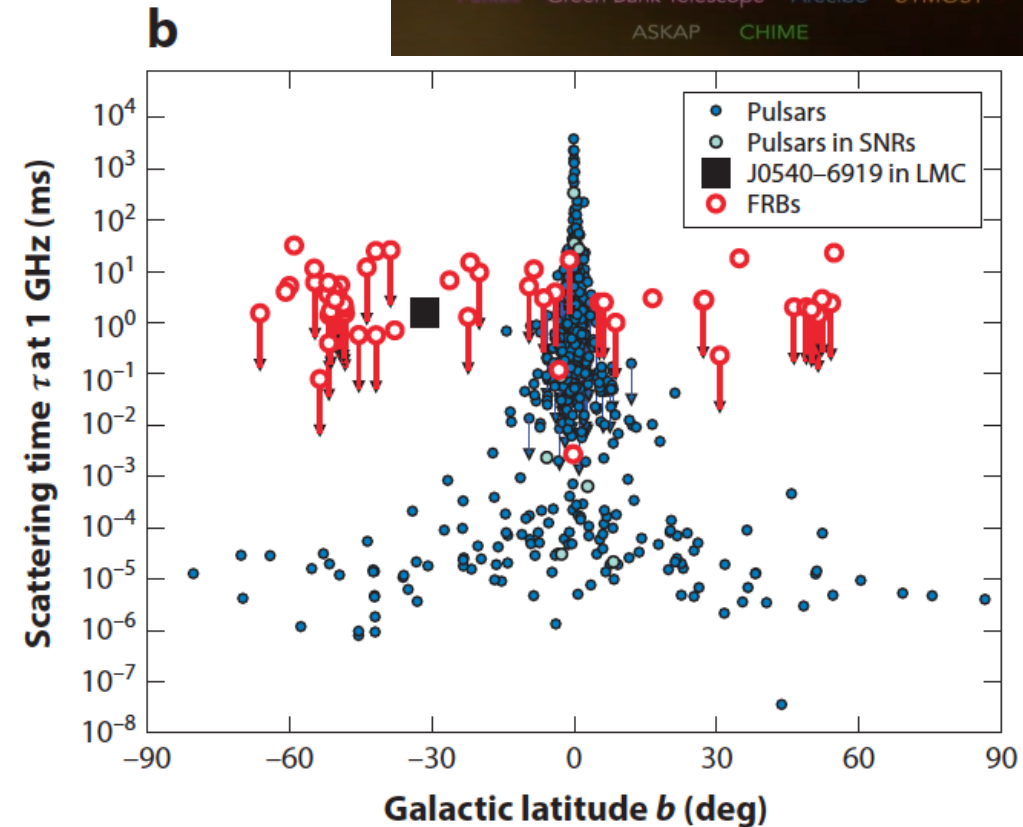
- ➤ Zero order tool to estimate distance
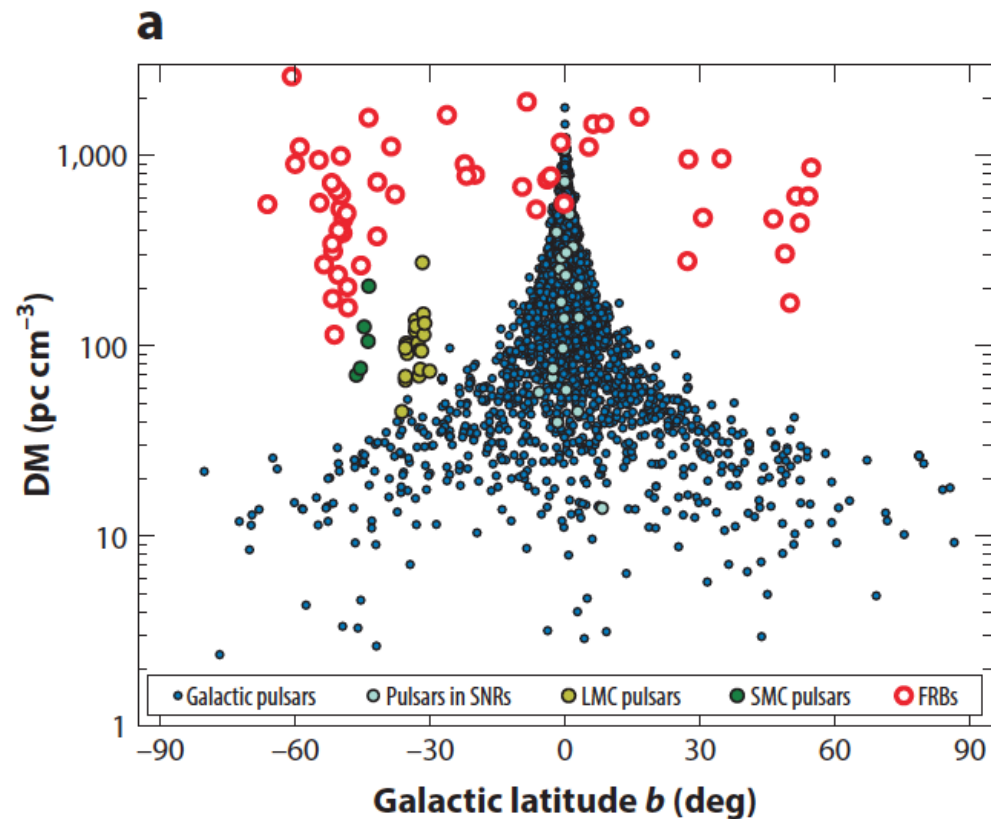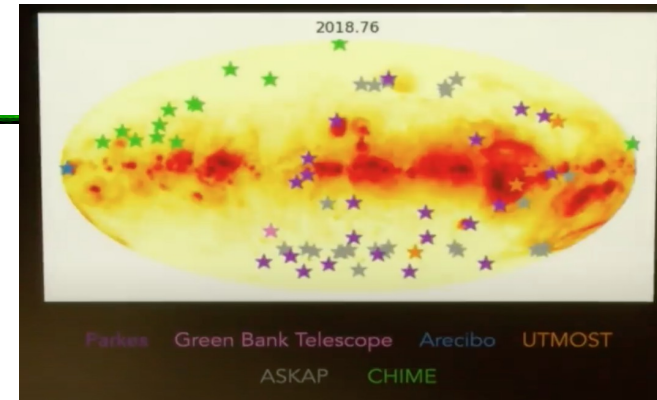
Figure 4

(*a*) Dispersion measures plotted against Galactic latitude for pulsars and FRBs. Different symbols are used for Galactic pulsars (2,422 objects), Galactic pulsars associated with SNRs (27), pulsars in the LMC (21) and SMC (5), and FRBs (55). (*b*) Scattering times for pulsars and FRBs at 1 GHz plotted against Galactic latitude. There are 421 pulsar measurements and 93 upper limits on τ compared with 18 FRB measurements and 37 upper limits. In panel *a*, DM measurements and pulsar associations were obtained from Manchester et al. (2005; **http://www.atnf.csiro.au/research/pulsar/psrcat**). Abbreviations: DM, dispersion measure; FRB, fast radio burst; LMC, Large Magellanic Cloud; SMC, Small Magellanic Cloud; SNR, supernova remnant.

Table 3 Polarization of FRBs

FRB	% Linear	% Circular	RM (rad m^{-2})	DM (pc cm^{-3})	$\Delta\psi$ (deg)	References
110523	44 ± 3	23 ± 30	-186 ± 14	623	~ 40	Masui et al. (2015)
121102	100	0	1.03×10^5	560	<10	MJD 57747, Michilli et al. (2018)
			0.93×10^5		<10	MJD 57991
140514	0 ± 10	21 ± 7	ND	563	ND	Petroff et al. (2015a)
150215	43 ± 5	3 ± 1	1.5 ± 10.5	1,106	<20	Petroff et al. (2017a)
150418	8.5 ± 1.5	0 ± 4.5	36 ± 52	776	~ 70	Keane et al. (2016)
151230	35 ± 13	6 ± 11	0	960	ND	Caleb et al. (2018)
150807	80 ± 1	ND	12 ± 0.7	267	<20	Ravi et al. (2016)
160102	84 ± 15	30 ± 11	-221 ± 6	2,596	$\lesssim 10$	Caleb et al. (2018)
180301	~ 30	~ 70	$-3,100$	520	$\lesssim 20$	Price et al. (2018)
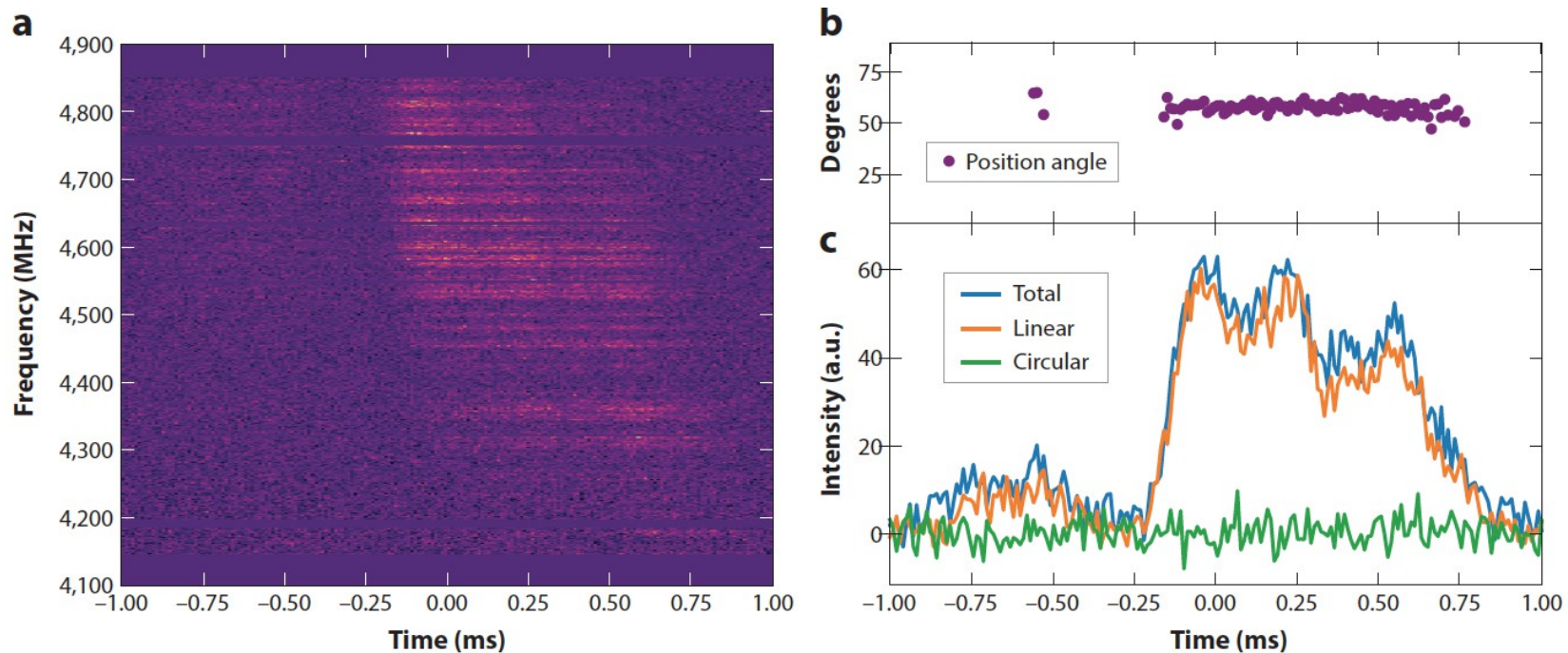
Figure 11

Dynamic spectrum, polarization angle, and pulse profile of a burst from FRB 121102 detected at Arecibo. (*a*) The burst dynamic spectrum, showing the fine structure in time and frequency. (*b*) The polarization position angle across the burst. (*c*) Total intensity (*blue*), linear polarization profile (*orange*), and circular polarization profile (*green*) for the burst. The burst is almost completely linearly polarized, with a constant polarization position angle. Figure based on observations by Michilli et al. (2018).
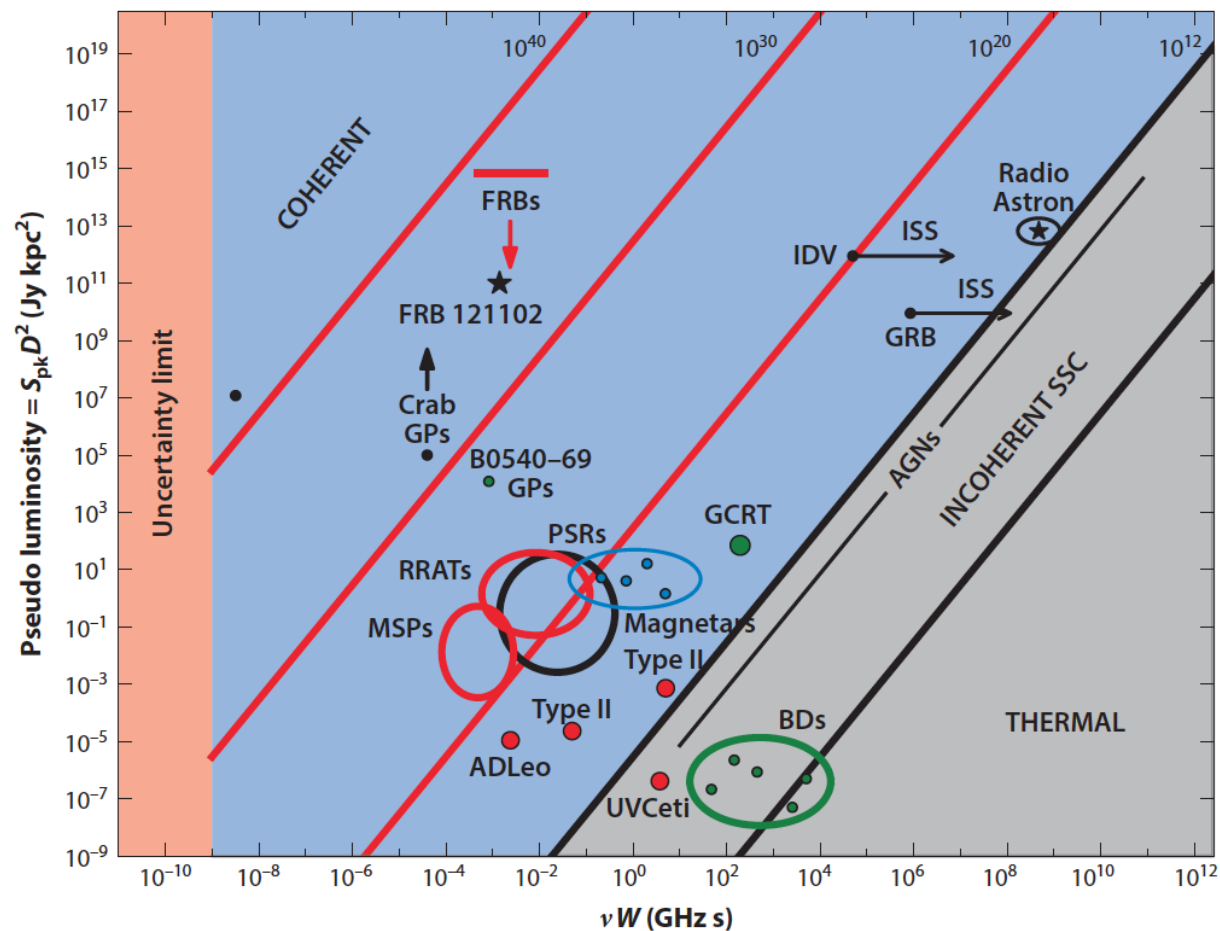
Figure 5

Time-luminosity phase space for radio transients showing the product of peak flux S_{pk} in Janskys and the square of the distance D in kiloparsecs versus the product of frequency ν in gigahertz and pulse width W in seconds. The "uncertainty" limit on the left indicates that $\nu W \gtrsim 1$, as follows from the uncertainty principle. Lines of constant brightness temperature $T_b = SD^2/2k(\nu W)^2$ are shown, where k is Boltzmann's constant. Points are shown for the nanoshots (Hankins & Eilek 2007) and GPs detected from the Crab pulsar and a few millisecond pulsars, and single pulses from other pulsars. Points are shown for solar bursts, radio flares from stars, brown dwarfs, and AGNs. The regions labeled "coherent" and "incoherent" are separated by the canonical $\sim 10^{12}$-K limit for the synchrotron self-Compton process occurring in AGNs. Arrows pointing to the right for the GRB and IDV points indicate that ISS implies smaller brightness temperatures than if characteristic variation times are used to estimate the brightness temperature. Fast radio transients include RRATs (McLaughlin et al. 2006), the GCRT source J1745-3009 (Hyman et al. 2005), and radio emission from Galactic magnetars (Olausen & Kaspi 2014). Abbreviations: AGN, active galactic nucleus; BD, brown dwarf; FRB, fast radio burst; GCRT, Galactic center radio transient; GP, giant pulse; GRB, gamma-ray burst; IDV, intraday variable; ISS, interstellar scintillation; MSP, millisecond pulsar; PSR, pulsar radio source; RRAT, rotating radio transient; SSC, synchrotron self-Compton.

➢ Summary of observed properties

➢ Isolated pulses from extragalactic objects
   (For more than 10 yr ,only one FRB was known to repeat. All others follow-up did not end with detections)
   (Nowadays, there are several repeaters)

➢ Short duration (~ms, possible broadening from scattering)
   Implications on the size of the region producing the energy

➢ Very high energy output
   Fluence, integrated over frequency and divided by duration (which is very short!)

➢ Very high brightness temperatures
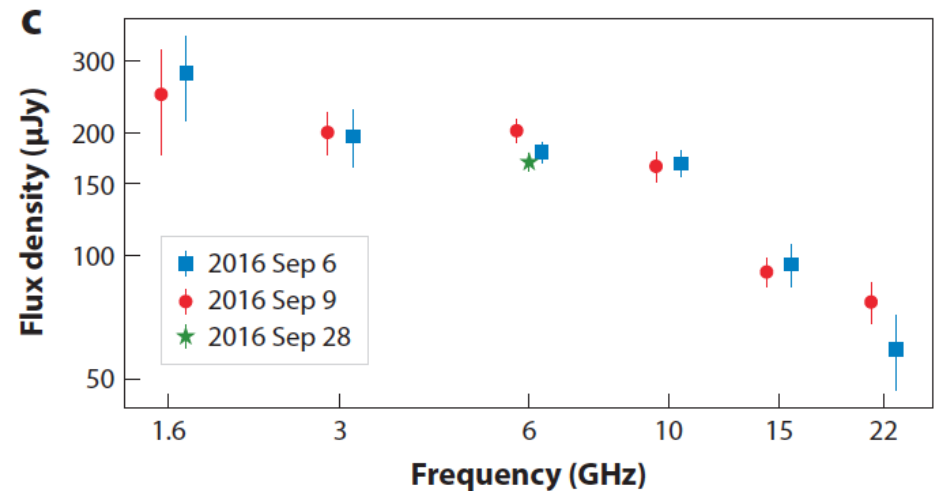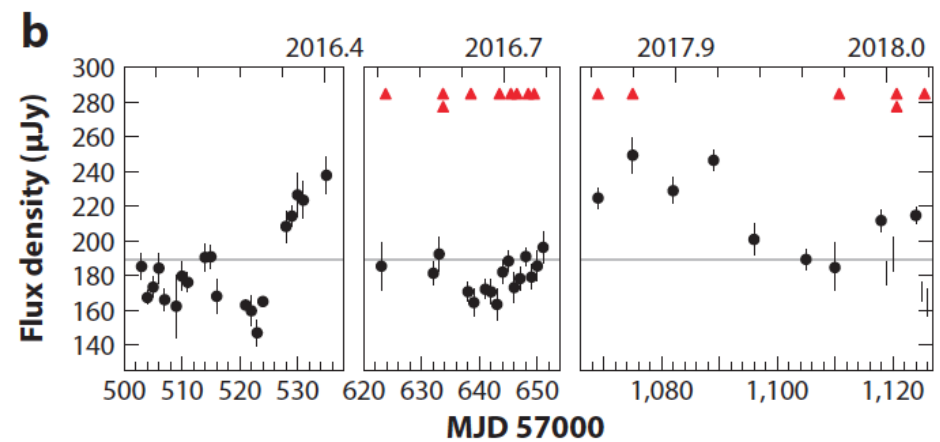   (Coherent mechanisms)

➢ Polarized emission in many FRBs
   (Linear and circular. A few RM are available)

➢ To be distinguished from perytons (microwave window early opening)

FRB121102

- First repeater known
- Persistent emission (localization!)
- Z=0.19 !

- Now more than a dozen of repeaters known
- Hundreds of FRBs in catalogue
  (http://www.frbcat.org).

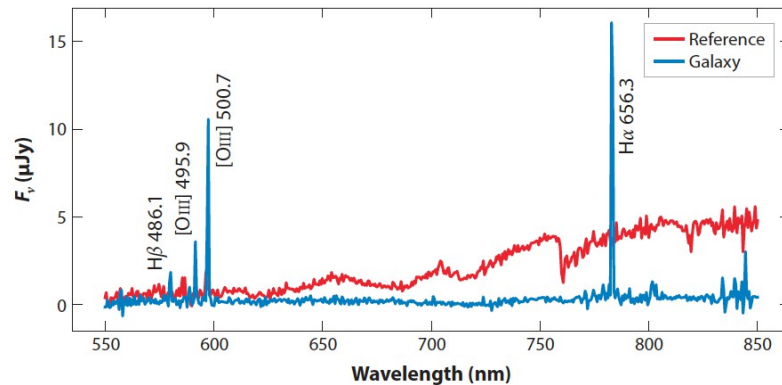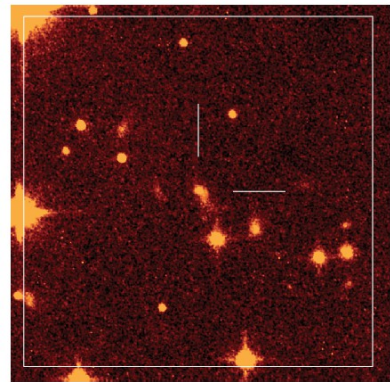FRB121102 @ VLA (black bullets are persistent emission, red triangles are FRBs detections)

Figure 10

(*a*) Image from the HST/WFC3 in the F110W filter (equivalent to J-band) showing the resolved irregular dwarf galaxy host of FRB 121102 (Bassa et al. 2017). A prominent knot of star formation dominates the optical emission. Lines indicating North and East are 3 arcsec in length. (*b*) The spectra of the host galaxy and the reference object (Tendulkar et al. 2017). Prominent emission lines are identified and labeled with their rest-frame wavelengths in nanometers, demonstrating the redshift of the galaxy. Abbreviations: FRB, fast radio burst; HST, *Hubble Space Telescope*; WFC3, Wide Field Camera 3.

One-shot (cataclismic) models:

- Blitzar (highly rotating NS, with $M > M_{OV}$);
  When rotation slows down via magnetic dipole spindown, NS collapses into BH; detached B field reconnects outside EH. Large current originates strong shock & super intense e-m emission [<1% of NS have to be supermassive to have the observed FRB rate (Falcke & Rezzolla 2014)].

- Binary NS-NS merger (B fields synchronized to binary rotation, radiation flash @ merging into BH) Curvature radiation

- Binary WD merger

Recurrent model(s):

- Magnetars
  Episodic events within/around the magnetar can produce the observed FRBs.

A bright millisecond-timescale radio burst from the direction of the Galactic magnetar SGR 1935+2154

332.81 pc/cc

At 2020-04-28 14:34:33 UTC (topocentric arrival time at 400 MHz) the CHIME/FRB backend (CHIME/FRB Collaboration et al. 2018 ApJ, 863, 48) detected a bright radio burst from the direction of SGR 1935+2154, a Galactic magnetar known to be in an active state (GCN #27657, ATels #13675, #13678, #13679).
The burst had a DM of 332.8 pc/cc. [...]
The radio burst was detected in multiple CHIME/FRB beams. This, and the frequency structure seen in the dynamic spectrum plot available at the URL provided below) indicate that the burst was detected **in a far side lobe**. Based on a frequency-dependent model of the synthesized CHIME/FRB beams fit to the detected spectra, we Localize the event to RA (deg) = 293.9, Dec (deg) = 22.1, 0.3 deg from the position of SGR 1935+2154, which was 21 deg from the CHIME meridian at the time of the burst. [...]

The burst had a double-peak structure with two components ~5 ms wide separated by ~30 ms [...] ...caution are not corrected for the telescope sidelobe response or instrumental bandpass. However, we do not expect the telescope's spectral response to change significantly on a timescale of 30 ms (the separation of the two bursts), which suggests that the two peaks indeed had different spectra. There is clear evidence for a scattering tail of similar magnitude in the two peaks. [...] However, accounting for our best estimate of the telescope response at that location, **we estimate the 400-800 MHz radio fluence to be a few kJy ms.**
If confirmed, this would be the first radio detection of SGR 1935+2154. Previous observations of this source [...]yielded upper limits of 0.4 mJy and 0.2 mJy [...] about 0.07 mJy and 0.1 mJy, respectively. Younes et al. (2017, ApJ, 847, 85) reported upper limits of 14 uJy and 7 uJy at 4.6 and 1.4 GHz, respectively. A preliminary search of the CHIME/FRB data since it commenced operations in late 2018 has revealed no past events from the source in spite of approximately daily ~10-min exposures. That the bright radio burst is seen at the time of particularly high X-ray activity from SGR 1935+2154 lends further credence to the association.
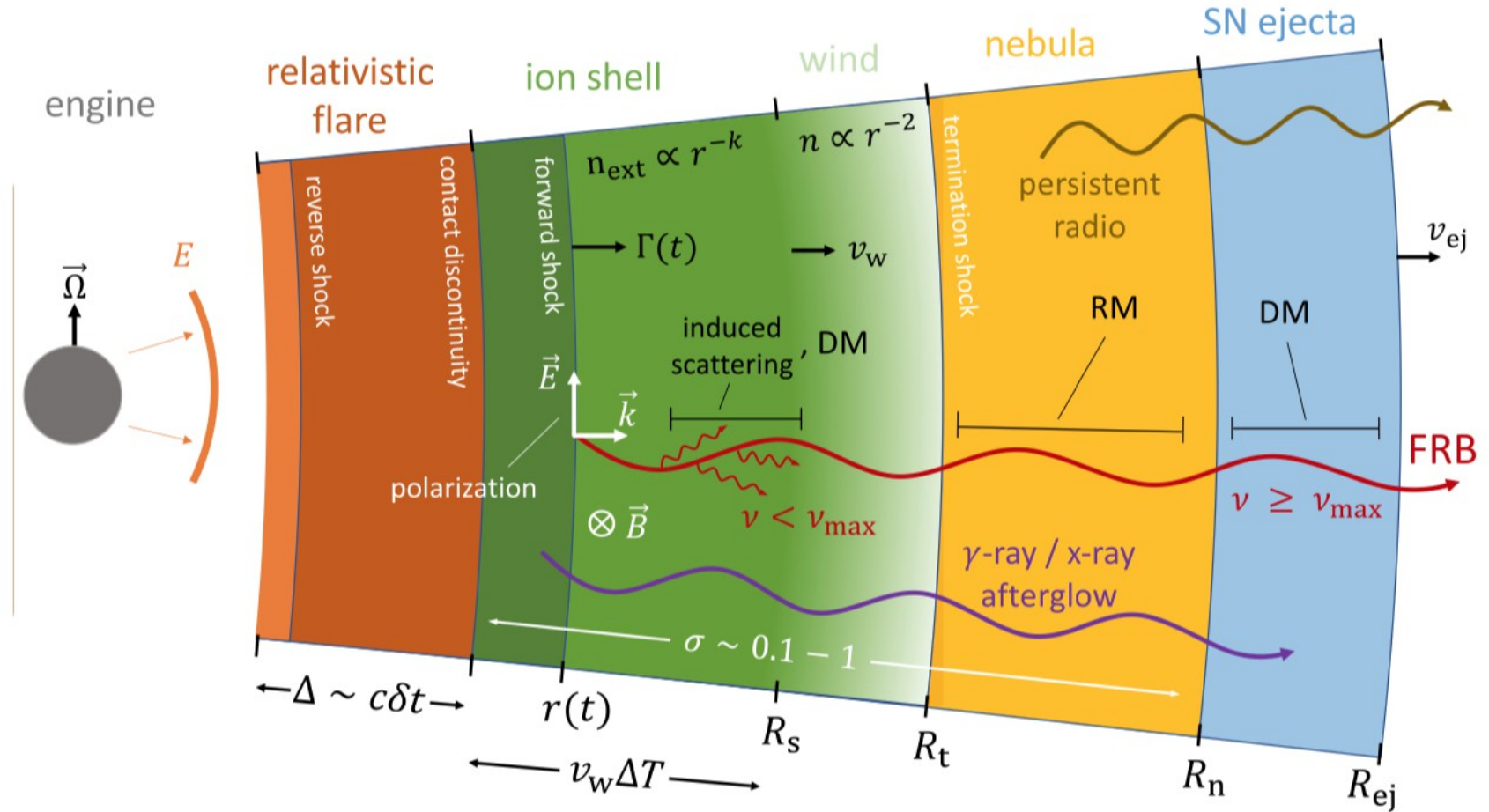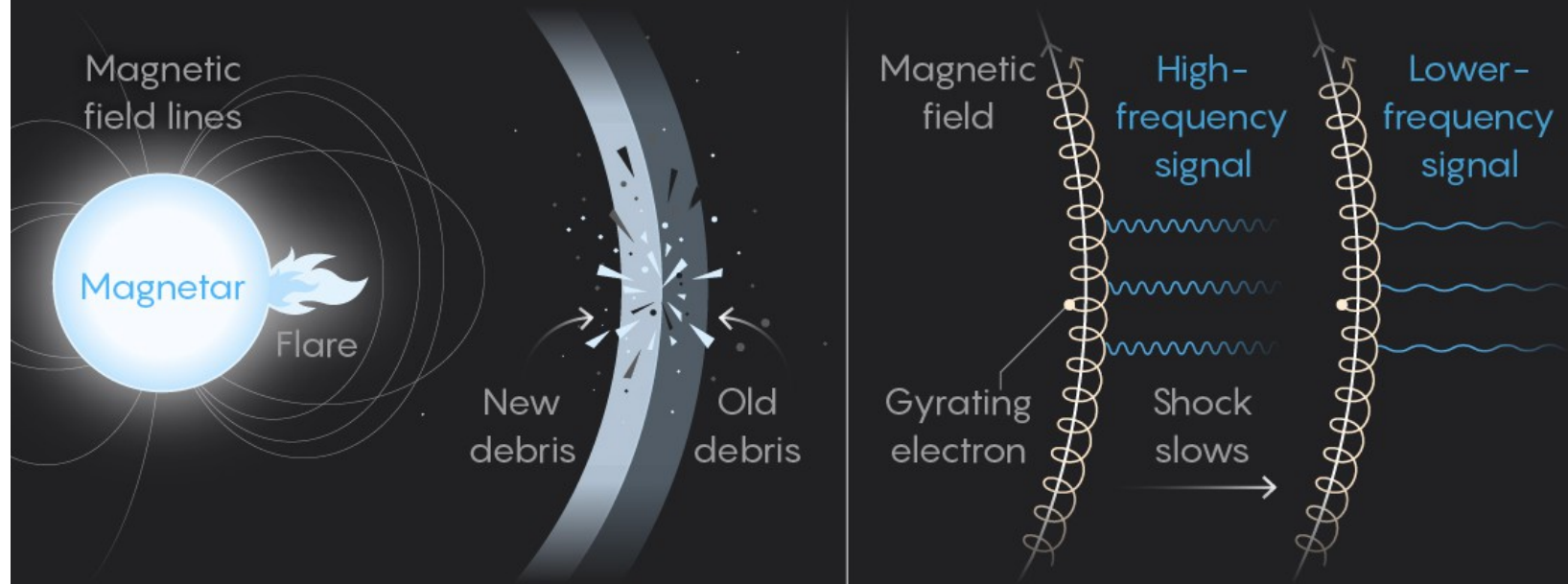
https://chime-experiment.ca/en
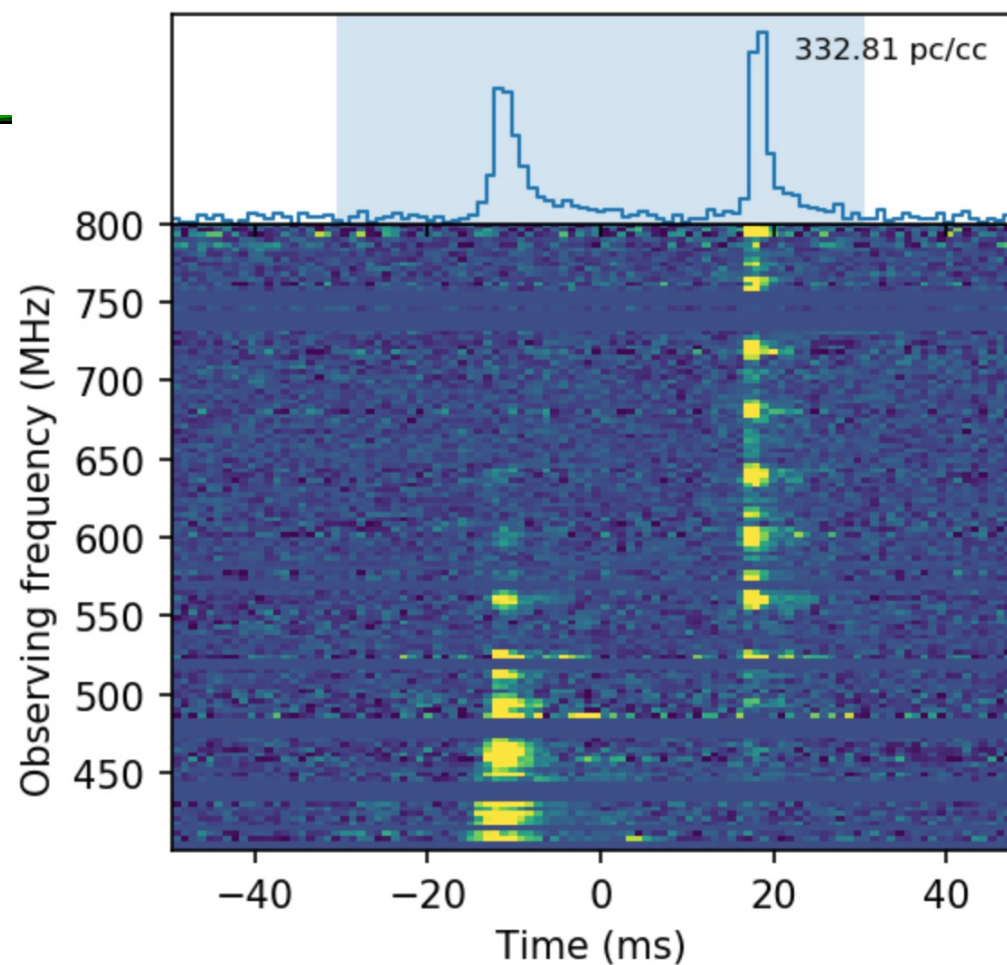
Figure 1. Radial scales and physical processes surrounding a repeating FRB source as described in this paper. The central engine releases an ultrarelativistic shell of energy E, duration $\delta t \lesssim 1$ ms, and radial width $c\delta t$, which collides with a mildly relativistic magnetized ion–electron shell of velocity v_w, baryon density $n_{ext} \propto r^{-k}$, magnetization $\sigma \sim 0.1$–1, and total width $v_w \Delta T$, as released following the previous major flare a time ΔT ago. The shell decelerates through reverse and forward shocks (Section 2), the latter of which produces the observed coherent radio emission (FRB) through the synchrotron maser mechanism (Section 3; Fig. 2). The upstream magnetic field $\vec{B}$ is wrapped in the toroidal direction perpendicular to the rotation axis Ω of the central engine, resulting in linear polarization of the FRB emission along the direction of Ω. The radio pulse is attenuated in the ion shell by induced Compton scattering at low frequencies $\nu < \nu_{max}$ (Section 3.1; equation 47). As the blast wave decelerates, the decreasing Lorentz factor Γ of the shocked gas and the reduced scattering optical depth of the upstream medium results in a downward drift of ν_{max} over the duration of the observed burst (Fig. 4). The forward shock also heats electrons to ultrarelativistic temperatures, powering (incoherent) synchrotron X-ray/gamma-ray emission, similar to a GRB afterglow (Section 4; Fig. 8). On larger scales, the train of ion shells from consecutive flares merges into a wind that feeds the nebula through a termination shock. Electrons injected at the termination shock powers the persistent radio source and (after cooling) generates the large rotation measure of the bursts. Stochastic or secular variation in the burst DM can also arise from the ion shell (on time-scales of $\Delta T \lesssim$ days) or from photoionization of the supernova ejecta by the flare X-rays (on time-scales of the source age of years to decades).

How Fast Radio Bursts Work

Fast radio bursts are brief, energetic blips of radio waves. A recent theory suggests that they come from a shock wave created by a magnetar.

Magnetic field lines

Magnetar

Flare

New debris   Old debris

Magnetic field   High-frequency signal   Lower-frequency signal

Gyrating electron   Shock slows

1 A magnetar releases a flare of electrons and other charged particles.

2 The flare collides with the remnants from an old flare, creating huge magnetic fields.

3 In the ensuing shock, gyrating electrons generate energetic radio waves. As the shock slows, the radio signal downshifts to lower frequencies.

However, in SGR 1935+2154, the low frequency signal arrives earlier than the high frequency one
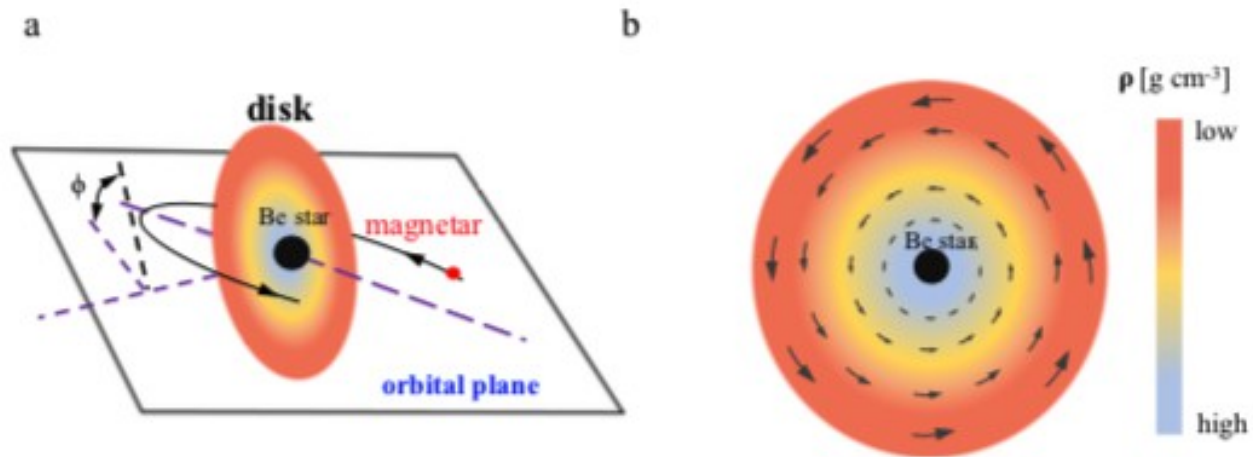
Fig. 1 A schematic diagram of the magnetar/Be star binary model. a The Be star locates at the center of the disk. The magnetar is shown as the red point. The stellar disk plane (shown as the black dash line) is inclined to the orbital plane (shown as purple dash lines) with the angle $\phi = \pi/12$. The purple dash line is the major axis of the magnetar's orbit. When the pathways of radio bursts pass through the disk, the interaction between bursts and disk can reproduce the observed variable rotation measure, depolarization, large scattering timescale, and Faraday conversion. **b** The face-on view of the Be star's disk. The magnetic field shown as arrows is assumed as azimuthal (or toroidal) in the disk. This model predicts that the RM contribution from the disk changes sign when the magnetar passes in front of the Be star. The RM variation discovered by FAST supports this scenario.

Wang et al. 2022, Nat Comm

Variations of the RM and DM can be attributed to a changing LoS during the orbiting period and the Magnetar can be in front/behind the "decretion" disk (debris from the explosion of the star that originated the magnetar and that have been captured by the gravity of the Be companion star). When some material from the disk goes to the magnetar, a burst can be originated.

The Northern Cross Fast Radio Burst project - II. Monitoring of repeating FRB 20180916B, 20181030A, 20200120E and 20201124A

M. Trudu[1,2]*, M. Pilia[2], G. Bernardi[3,4,5], A. Addis[6], G. Bianchi[3], A. Magro[7], G. Naldi[3], D. Pelliciari[3,8], G. Pupillo[3], G. Setti[3,8], C. Bortolotti[3], C. Casentini[9,10], D. Dallacasa[3,8], V. Gajjar[11], N. Locatelli[12], R. Lulli[3], G. Maccaferri[3], A. Mattana[3], D. Michilli[13,14], F. Perini[3], A. Possenti[1,2], M. Roma[3], M. Schiaffino[3], M. Tavani[9,15] and F. Verrecchia[16,17]
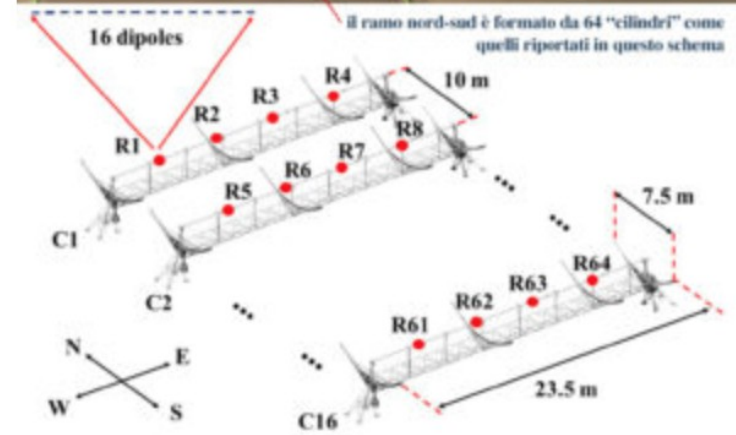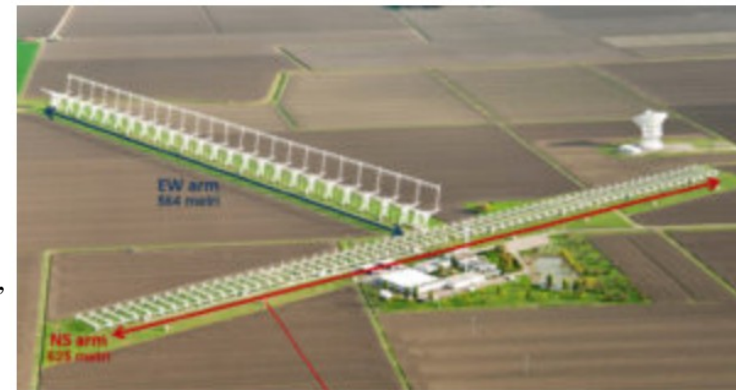
Above, aerial view of the Medicine Station, with the two perpendicular branches of the Northern Cross. Below, diagram of the "cylinders" that form the north-south branch. Source: N. Locatelli et al. Mnras, 2020

Left: Germano Bianchi learns from Maura Pilia about the first detection of a fast radio burst by the Northern Cross. Right: Bianchi, Pilia and Gianni Bernardi celebrate the result on Skype.